8-21-2017

Electronic Structure and Vibrational Behavior of Polyethylene: Role of Chemical, Morphological and Interfacial Complexity

Lihua Chen
University of Connecticut - Storrs, lihua.chen@uconn.edu

Electronic Structure and Vibrational Behavior of Polyethylene: Role of Chemical, Morphological and Interfacial Complexity

Lihua Chen, Ph.D.

University of Connecticut, 2017

ABSTRACT

The electronic structure and vibrational behavior of a polymeric insulator encode essential signatures of its short-term electrical performance and long-term reliability. A critical long-standing challenge though is that key features of these two properties of a polymeric insulator (and its evolution) under realistic conditions have not been entirely accessible, either via experimental or computational approaches, due to the inherent complexities involved. In this comprehensive study, the role of chemical and morphological imperfections that inevitably exist within the technologically important prototypical and pervasive insulator, polyethylene (PE), and at electrode/PE interfaces, has been investigated. Large-scale density functional theory computations and long-time molecular dynamics simulations were employed to accurately recover, explain and unravel a wide variety of experimental data obtained during

the electrical degradation of PE. This scheme has allowed us to directly and realistically address the relationships between physico-chemical structures and the relevant properties (i.e., the electronic structure and vibrational behavior) of PE. These efforts take us a step closer to understanding and potentially controlling dielectric degradation and breakdown.

Electronic Structure and Vibrational Behavior of Polyethylene: Role of Chemical, Morphological and Interfacial Complexity

Lihua Chen

M.S., North China Electric Power University, China, 2013

B.S., North China Electric Power University, China, 2010

A Dissertation

Submitted in Partial Fulfillment of the

Requirements for the Degree of

Doctor of Philosophy

at the

University of Connecticut

2017

APPROVAL PAGE

Doctor of Philosophy Dissertation

Electronic Structure and Vibrational Behavior of Polyethylene: Role of Chemical, Morphological and Interfacial Complexity

Presented by

Lihua Chen, M.S., B.S.

Major Advisor _____
Rampi Ramprasad

Associate Advisor _____
Yang Cao

Associate Advisor _____
Avinash M. Dongare

University of Connecticut

2017

ACKNOWLEDGMENTS

I am very grateful to my major advisor Prof. Rampi Ramprasad, for his great advice, persistent support and patience. Without his help, it would have been difficult for me to achieve my Ph. D degree. I learned a lot from him, not only technical skills such as computational techniques, writing, and presenting, but also soft skills like communications, teamwork and time management. These will benefit me for life.

I also appreciate my associate advisors Prof. Avinash M. Dongare and Prof. Yang Cao for their kind help and valuable suggestions, which have been important to my research. In addition, I would like to acknowledge Prof. Steven Boggs, who has provided significant advice not only for my research but also for my career development.

Many thanks to the current and previous group members for their valuable assistance on my research, especially, Dr. Huan Tran, Dr. Chenchen Wang, Dr. Chiho Kim and Dr Yenny P. Cardona Quintero. I also would like to say thanks for the help from other group members and friends in Uconn, including Dr. Hom Sharma, Dr. Venkatesh Botu, Dr. Arun Kumar Mannodi Kanakkithodi, Rohit Brata, Mingwan Zhang and Changmin Hu.

I am deeply grateful to my family for all their support. They enabled me to choose my path, and also gave me the inspiration to overcome the difficulties I encountered. I really appreciate their love, help, and understanding.

Finally, the financial support of this work from a Multi-University Research Initiative (MURI) grant of Naval Research and computational support from Extreme

Science and Engineering Discovery Environment (XSEDE) are gratefully acknowledged.

TABLE OF CONTENTS

LIST OF TABLES

LIST OF FIGURES

Chapter 1

Introduction

1.1 Polymeric Insulators

Polymers are important insulating materials in electronic and electrical domains, due to their superior electronic and thermal properties [1]. For example, polyethylene has been used as an insulator for high-voltage cables [1, 2], and other polymers including polypropylene, polystyrene and poly(vinylchloride) have served as dielectrics for film capacitors since 1960s [3–5]. In recent decades, polymers have been utilized as gate dielectrics for field effect transistors, e.g., cross-linked polystyrene [6, 7]. Compared with traditional inorganic insulators such as SiO_2, polymers are flexible, low-cost and can be manufactured easily [1]. However, the insulating behavior of polymers becomes progressively (and in many cases, irreversibly) degraded over time, especially when they are exposed to air, heat, UV and the high electric field encountered during operation. This process ultimately leads

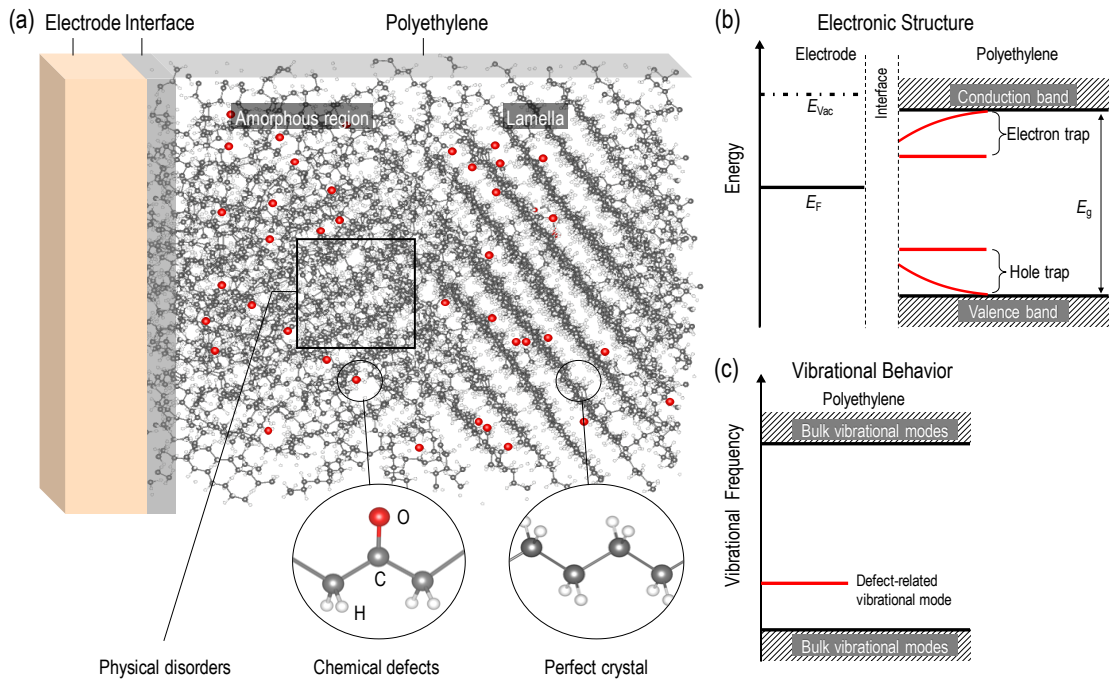

Figure 1.1: Schematic structure of electrode/polyethylene interfaces, containing crystalline and amorphous regions, and populations of chemical defects. Here, C, H, and O atoms are shown in black, white, and red, respectively. (b) Electronic structure of electrode/polyethylene interfaces and bulk polyethylene with imperfections. E_{vac}, and E_{F} are the vacuum level and the Fermi level of metal, respectively. Red lines are energy states induced by defects/disorder. (c) Vibrational behavior of polyethylene including defects/disorder.

to dielectric breakdown, the event by which the material sharply loses its insulating characteristics [8–11].

According to extensive experimental and computational studies, the degradation of insulating behaviors of polymers is related to various "imperfections" within polymers, in addition to the electric field induced factors, such as partial discharges and electrical/water trees, etc. [8–11]. These imperfections within polymers can degrade their electronic structure and vibrational density of states, which can increase the electron transport and decrease the heat transport across the polymers. More importantly, excitons and free charge carriers can become localized at such defects, initiating chemical reactions, e.g., the bond breakage and the formation of

new defects. Consequently, the electronic and vibrational structure of polymers are further degraded, leading to electron avalanches and dielectric breakdown [8, 11]. These issues are addressed separately below.

1.1.1 Electronic structure of polymers

Perfect, defect-free, single-crystalline "good" insulators, such as polyethylene, that have majestic band gaps of over 8 eV can display very low intrinsic conductivity about 10^{-45} S/m [12]. However, various types and classes of imperfections degrade the electronic structure. Real materials, especially polymers, are never single-crystals, nor are they devoid of chemical imperfections in the bulk or close to interfaces with other materials (e.g., electrode metals), as shown in Fig. 1.1 (a) for the case of polyethylene. Such imperfections translate to features in the electronic structure, such as defect or "trap" states within the band gap, alteration of the band edge positions leading to a decrease of the effective band gap, and undesirable degrees of offsets between band edges across interfaces (e.g., between the insulator and an electrode) [8, 12, 13], as portrayed in Fig. 1.1 (b). These factors enhance both charge injection into the insulator (from electrodes) and charge transport within the insulator [8, 12]. For example, the electrical conductivity of the electrical grade commercial XLPE is in the range of 10^{-16} – 10^{-14} S/m [8].

1.1.2 Vibrational behavior of polymers

In addition to modification of electronic structure, defects/disorder can introduce high/low-frequency vibrational modes (see Fig. 1.1 (c)). Such frequencies can

be measured by Infrared (IR) and Raman spectroscopy, or photo-luminesences [14], which can be used to track the degradation of polymers. For example, the carbonyl defect (C=O) has been observed in polyethylene with an IR absorption band at 1,720 cm^{-1} [14]. Further, for polymers, the thermal energy is transfered by lattice vibrations (i.e., phonons). Defect-induced vibrational modes lead to an increase in the phonon scattering rates, thereby resulting in a decrease in the thermal conductivity of the polymer. This may impede the heat flow within polymers. The accumulated energy can result in further defect formation due to the breakage of additional bond [8].

Based on these considerations, it is important to understand the relationships between physico-chemical structures and the relevant properties (i.e., the electronic structure and vibrational behavior) of polymers. These investigations will not only take us a step closer to understand and prevent the electric degradation of polymers, but also may assist in the rational design of novel polymers with desired electrical properties.

1.2 Challenges with Polyethylene

Among polymeric insulators with the large band gap, polyethylene (PE) is selected as the model insulator, due to its simple structural repeat unit (–CH_2–) and wide applications. Despite extensive experimental and computational efforts have been performed to probe its physical, chemical and electronic structures [12,13,15–22], a clear understanding of the electronic structure and vibrational

behavior of "realistic" PE is still not at hand. One of the main reasons is that the physical structure of "realistic" PE is very complex.

A snapshot of a "realistic" situation for the case of PE interfacing with a metallic electrode is portrayed in Fig. 1.1 (a). Bulk PE, as most polyolefins, is a mixture of amorphous and crystalline (within lamellas) regions [1]. Evidence from IR spectra indicates that a variety of localized morphological imperfections, e.g., kinks [14] and branches (methyl groups) [1], and chemical defects such as carbonyl (C=O) [23–25], are present in PE (see Table 1.1). This complicated "blend" evolves during and post processing. The complexity of PE makes it difficult to unambiguously determine the energy levels caused by defects and interfaces by experiments, e.g., luminescence spectroscopy, device-level current-voltage characteristics, and the pulsed electro-acoustic method [23–27].

Table 1.1: Available experimental IR, photo-, electro- and thermo-luminescences (denoted by PL, EL, and TL, respectively) of disorder/defects in PE.

Disorder/defects	IR (cm^{-1})	Luminescence centers (eV)
Branches-methyl	2962[a]	
Gauche, kinks, fold chains	1300 – 1400[b]	
C=C	888[c]	
C=CH_2	909[c]	4.13 – 6.02 (TL)[f]
C–OH	3371[c]	
C=O	1720[c]	2.06 – 3.10 (PL); 2.92 (EL)[g]
O–C–O	1735[c]	
HO–C=O	1713[c]	
C–O–C	1253/908/842[d]	
C–X (X=Cl, Br, I)	515 – 815[e]	

[a]Ref. [1]; [b]Ref. [14]; [c]Ref. [23, 24]; [d]Ref. [25]; [e]Ref. [28]; [f]Ref. [27]; [g]Ref. [26]

Computations, e.g., first principles based on density functional theory (DFT) [30, 31] and molecular dynamics (MD) with classical force fields [32, 33], provide atomic-level understanding and insights of PE [12, 17, 20, 21]. Past DFT work on

Table 1.2: Summary of trap depths calculated with *ab-initio* simulations.

Disorder/defects		Trap depth (eV)	
		For electrons	For holes
Chemical Defects	In-chain C=O	1.96[a]; 1.40[b]	0.95[a]; 0.71[b]
	End-chain C=O	1.69[b]	0.57[b]
	End-chain C=OH	0.04[b]	0.41[b]
	In-chain C=CH2[a]	0.97[a]; 0.31[b];	1.0[a]; 0.35[b]
	In-chain C=C[a]	1.06[a]; 0.22[b]	1.06[a]; 0.78[b]
	In-chain C=C–C=C	1.85[a]; 1.86[b]	1.53[a]; 1.84[b]
	Acetophenone	2.28[b]	0.71[b]
	Alpha-methylstyrene	1.79[b]	0.67[b]
	Cumene	0.98[b]	0.56
	Cumyl-alcohol	1.14[b]	0.54[b]
	Water	0.36[b]	-
Physical disorders	Lamella	0.39[c]	-
	Amorphous	0.27[c]	-

[a] Ref. [20]; [b] Ref. [29]; [c]Ref. [21]

PE focused mainly on electronic structure, using either electron affinity differences of PE with and without defects [29, 34], or Kohn-Sham eigenvalues computed by the use of (semi)local exchange-correlation functionals [20, 35]. DFT calculations related to the electronic structure of metal/PE interfaces and vibrational behavior of PE are still in a state of infancy [36].

The computed trap depths for various defects are summarized in Table 1.2. While past work provides a qualitative picture of the defect levels, the computations were based on early implementations of DFT that underestimated significantly the band gap which caused some ambiguity in the determination of energy levels relative to the band edges. In addition, computations have not been easy to perform at the requisite level of theory for the morphologically complex PE, and so are typically undertaken for parts of (idealized versions of) the real system [12, 17, 20, 21]. For example, some large-scale physical disorder, e.g., amorphous regions, have been

generated with classical MD simulations and then used to compute the electronic structure with DFT. However, this is limited by the accuracy of the force field adopted [21].

1.3 Objective of This Research

This dissertation aims to fill the above gap by charting *comprehensively* the electronic structure and the vibrational density of states of realistic PE, inclusive of a majority of its physico-chemical complexity at one consistent (and high) level of theory using state-of-the-art large scale DFT calculations and classical MD simulations. The following issues have been addressed:

- Role of physical disorder and chemical defects in determining the electronic structure of PE;
- Investigation of the electronic structure of electrode/PE interfaces and implications for charge injection barriers at interfaces;
- Impacts of physical disorder and chemical defects on the vibrational density of states of PE.

The organization of this thesis is described briefly below.

- Chapter 2 introduces the computational methods used in this research, including density functional theory and classical force fields.
- Chapter 3 discusses the electronic structure of physical disorder in PE.

- Chapter 4 describes the electronic structure of chemical defects in PE.
- Chapter 5 presents the electronic structure of electrode/PE interfaces. Charge injection barriers at interfaces were computed, and the effect of metal work function, interfacial dipole moments and defects/disorder within PE are discussed.
- Chapter 6 provides a recap of the electronic structure calculations of PE.
- Chapter 7 shows the vibrational behavior of the physical disorder and chemical defects in PE.
- Chapter 8 summarizes all work discussed above and suggests the future work.

Chapter 2

Computational Methods

2.1 Introduction

In this work, density functional theory (DFT) and molecular dynamics (MD) simulations with classical force fields have been applied to investigate the electronic structure and vibrational behaviors of PE. The classical MD simulations are either used to generate initial structures of large-scale systems (more than 1200 atoms) that are adopted in the electronic structure calculations, or applied to estimate the vibrational frequencies of large-scale systems. This chapter aims to give an overview of these computational methods. First of all, methodologies used in DFT calculations are introduced, including a brief introduction to DFT and approaches to computing the electronic structure and related properties. Next, an introduction to MD protocols and classical force fields are presented, followed by force fields validation. Finally, the computational details used in all calculations are summarized.

2.2 Density Functional Theory Calculations

2.2.1 Introduction to density functional theory (DFT)

Density functional theory (DFT) based quantum mechanical methods are promising to predict the physical and electronic structures of materials with various geometric classes, such as molecules, bulk solids, surfaces and interfaces, etc. [30, 31]. The details of this theory have been well reviewed in the literature [37]. In particular, such method is parameter-free, also called "first-principles" or "*ab initio*" techniques. Fig. 2.1 shows DFT-computed structural parameters and various properties, e.g., band gap and vibration frequency. It can be seen that all of them except the band gap are captured accurately by the conventional DFT.

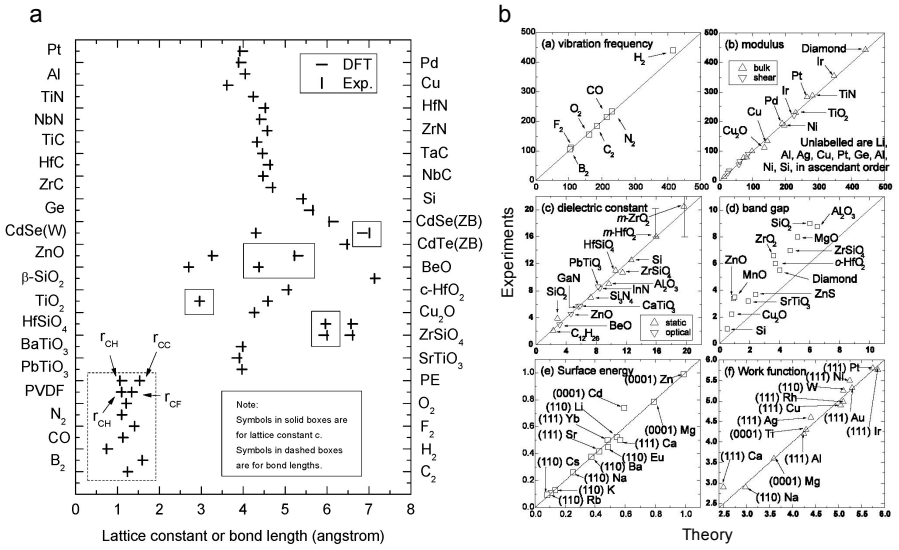

Figure 2.1: Comparison between DFT-computed structural parameters **a** and various properties **b** with experiments. Data are taken from Zhu's thesis [38].

2.2.2 Electronic structure calculations

The computed band gap in Fig. 2.2 b shows that there is a "band gap" problem for DFT with semi(local) functionals (e.g., the Perdew-Burke-Ernzerhof (PBE) functional). Therefore, beyond-DFT methods have been developed, e.g., the Heyd-Scuseria-Ernzerhof functional (HSE) and many body perturbation approximation (GW), to estimate the electronic structure and related properties [39]. As can be seen from Fig. 2.2, the GW method gives the best results, however, such method is very expensive for large systems (>100 atoms). Therefore, the HSE functional is applied in this work to study the electronic structure of PE.

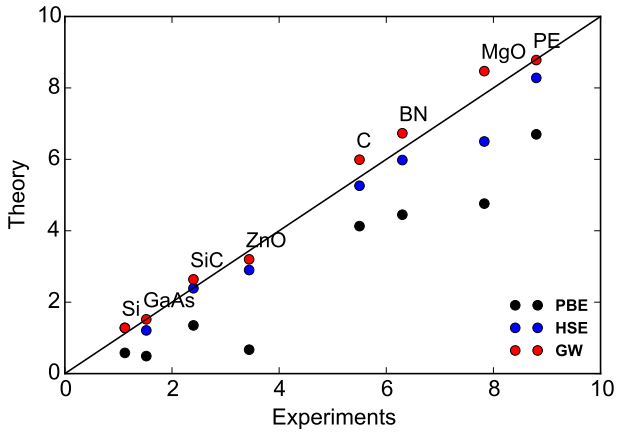

Figure 2.2: Band gaps computed with PBE, HSE, and GW methods, compared with experiments. Data are derived from Ref. [39].

To extract the electron and hole trap depths, i.e., E_t^e and E_t^h, Kohn-Sham eigenvalues, computed with the HSE functional, are corrected by aligning the average C-1s core level state in the defect-containing models with those of perfect PE. Original data points are provided in Table B.2 and B.3 of Appendix B. For large-scale

disorders, e.g., lamella, amorphous, and semi-crystalline, the hole trap depth $E_{\mathrm{t}}^{\mathrm{h}}$ was computed using the PBE XC functional, and the electron trap depth is obtained by $E_{\mathrm{g}}^{\mathrm{HSE06}} + E_{\mathrm{t}}^{\mathrm{h}}$, where $E_{\mathrm{g}}^{\mathrm{HSE06}}$ is the band gap estimated at the HSE06 level of DFT using Eq. (2.1). This relation was derived from $E_{\mathrm{g}}^{\mathrm{PBE}}$, the band gap calculated at the PBE level of DFT, and $E_{\mathrm{g}}^{\mathrm{HSE06}}$, both of them were computed for physical disorders in the crystal region (see Fig. 2.3). 50 data points were selected to cover a wide range of the band gap, including 1 from the perfect crystal, 19 from the density variation, 10 from the non-uniform bonds/angles, 10 from the gauche conformations, and 10 from the kinks. Original data points are available in Table B.4 of Appendix B.

$$E_{\mathrm{g}}^{\mathrm{HSE06}} = 1.1028 \times E_{\mathrm{g}}^{\mathrm{PBE}} + 0.689, R^2 = 0.99 \tag{2.1}$$

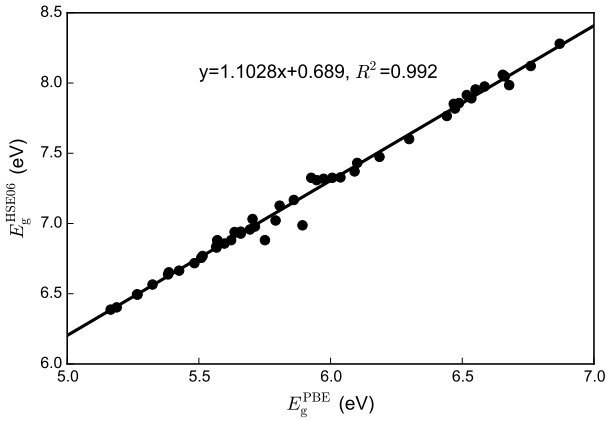

Figure 2.3: Relationship between $E_{\mathrm{g}}^{\mathrm{PBE}}$ and $E_{\mathrm{g}}^{\mathrm{HSE06}}$, derived from calculations of physical defects in crystal regions with PBE and HSE06 functionals.

2.2.3 Thermodynamic and optical transition levels

In order to unravel luminescence signatures, thermodynamic and optical transition levels of chemical defects were computed. Thermodynamic transitions (involving long time scales) will involve initial and final charge states at the respective equilibrium geometries. Optical transitions will occur at much shorter time scales, and will involve the final charge state at the equilibrium geometry of the initial charge states.

A formally correct approach to determine defect levels is via total energy differences of PE with defects at initial and final charge states [40–42]. In general, the thermodynamic transition levels $\mu(q/q')$ is the Fermi energy at which defects in two different charge states q and q' are at thermodynamic equilibrium and is given by [40–42]

$$E^{\text{therm}}_{(q/q')} = \frac{E^{\text{f}}_q(R_q) - E^{\text{f}}_{q'}(R_{q'})}{q - q'}. \tag{2.2}$$

Here, $E^{\text{f}}_q(R_q)$ is the formation energy of the q-charged defect at its equilibrium structure R_q, as defined by

$$E^{\text{f}}_q(R_q) = E^q_{def} - E_{per} \pm \eta + q(\mu + E_{ref} + \Delta V) + E^q_{corr}. \tag{2.3}$$

E^q_{def} and E_{per} are the DFT total energies of the supercells including defects at the charge state q and the perfect bulk, respectively. $\pm\eta$ is the chemical potential of atoms removed or added. E_{ref} corresponds the average local electrostatic potential (E_{av}) of PE far away from the defect location, and ΔV is the E_{av} difference of the supercells with and without the defect. The Fermi energy (μ) is taken from VBM to

CBM of defect-free PE. The electrostatic interactions of charged defects (E^q_{corr}) due to the periodicity and the finite supercell sizes are corrected by first-order monopole corrections in all defect cases considered [19].

In the case of optical transition, the atomic configuration of the defect at the initial charge state q is fixed even though charge transition exists. Because the optical transition depends on the direction of charge transfer, two kinds of optical energies are possible: emission energy (E_{e}) for charge transfer from initial state q to final state q' and absorption energy (E_{a}) for the reverse process. The method to determine the optical transition level is similar to the previous case, but the energy of the final state is computed using the equilibrium structure of the initial state. Therefore, the optical transition level from initial state q to final state q' is defined as

$$E^{\mathrm{opt}}_{(q\to q')} = \frac{E^{\mathrm{f}}_{q'}(R_q) - E^{\mathrm{f}}_{q}(R_q)}{(q'-q)}, \tag{2.4}$$

where $E^{\mathrm{f}}_{q'}(R_q)$ is the defect formation energy in the charge state q' corresponding to the equilibrium structure R_q of the initial charge state q.

2.2.4 Charge injection barriers computations

According to the energy-diagram of the metal/PE interface shown in Fig. 1.1 (b), due to the formation of interfacial dipole moments $\mathbf{D}$, the PE and metal vacuum levels are misaligned by $\Delta\varphi$, defined as [43, 44]

$$\Delta\varphi = -\frac{e\mathbf{D}}{\varepsilon_0 A}. \tag{2.5}$$

Here, ε_0 is the vacuum permittivity, e the electron charge, and A the area of Al/PE interface. **D** was computed by integrating the elementary dipole moment, obtained from DFT, over the whole system. The electron and hole injection barriers, i.e., ϕ_{e} and ϕ_{h}, are given by

$$\phi_{\mathrm{e}} = \psi_{\mathrm{m}} + \Delta\varphi - E_{\mathrm{ea}} - E_{\mathrm{t}}^{\mathrm{e}}, \tag{2.6}$$

$$\phi_{\mathrm{h}} = E_{\mathrm{g}} - E_{\mathrm{t}}^{\mathrm{e}} - \phi_{\mathrm{e}} - E_{\mathrm{t}}^{\mathrm{h}}. \tag{2.7}$$

Here, ψ_{m}, E_{g}, E_{ea}, $E_{\mathrm{t}}^{\mathrm{e}}$, and $E_{\mathrm{t}}^{\mathrm{h}}$ are the metal work function, the band gap of perfect PE, the electron affinity of the PE slab, the electron and hole trap depths, respectively. ψ_{m} and E_{ea} were computed with individual Al(111) and PE(110) slabs using the DFT-based approach called "bulk plus band lineup" method [45], agreeing with experimental values [22].

2.2.5 Vibrational density of states

Vibrational frequencies of small-scale systems (< 200 atoms) are computed with the finite displacement method (FDM) implemented in PHONOPY [46]. In addition to the total density of states (DOS), the local DOS ($ldos(\omega)$) with the Gaussian distribution is also used in this work, defined by

$$ldos(\omega) = \sum c_i g^i,\ i < r_{\mathrm{cut}}, \tag{2.8}$$

where g^i is the projected DOS of atom i [46]. c_i is the weight of atom i at position x and computed by Eq. (2.9)

$$c_i = \frac{1}{\sqrt{(2\pi\sigma)^3}} exp^{-\frac{r^2}{2\sigma^2}}. \tag{2.9}$$

Here, r is the distance between atoms and the gaussian center within a r_{cut} of 6 Å, and σ is the standard deviation with a value of 0.5 Å. Details of local DOS are shown in Appendix C.

2.2.6 Heat capacity

The heat capacity at constant volume (C_{V}), which is defined as

$$C_{\text{V}} = k_B \int_{\omega_{\min}}^{\omega_{\max}} d\omega g(\omega)(\frac{\omega}{k_B T})^2 exp(\frac{\omega}{k_B T})[\frac{\omega}{k_B T} - 1]^{-2}/N_{\text{CH}_2}. \tag{2.10}$$

Here, k_B is the Boltzmann constant and N_{CH_2} is the total number of CH_2 groups included in the systems.

2.3 Molecular Dynamics Simulations with Classical Force Fields

2.3.1 Molecular dynamics

Molecular dynamics (MD) is a computational technique to study the dynamical evolution of atoms and molecules [47]. The way to obtain the trajectories of atoms and molecules is by numerically solving Newton's equations of motion, defined as

$$F_i = m_i \frac{dv_i}{dt}, \tag{2.11}$$

$$v_i = \frac{dr_i}{dt}. \tag{2.12}$$

Here, F_i is the force of the i particle of mass m_i, position r_i and velocity v_i. F_i are determined by potentials $\Delta U(r_i)$ at the point r_i which describes interactions between particles of the system and the external force impacts, expressed as

$$F_i = -\Delta U(r_i). \tag{2.13}$$

2.3.2 Introduction to OPLS and reactive force fields

The definition of $\Delta U(r_i)$ is the key factor in MD simulations. The empirical interatomic potentials are also called force fields in the chemistry domain. One common empirical force fields used to model PE is OPLS-all atom [32, 48, 49]. In this force field, bonded interactions are computed with harmonic potential functions. Coulomb's law and Lennard-Jones potential function are used to estimate non-bonded charge interactions and van der Waal interactions, respectively. With these approximations, structural and conformational changes can be modeled, but chemical reactions can not be simulated. In this situation, reactive potentials are required, which can model bond formation and dissociation, such as reactive force field [33], and AIREBO [50].

Reactive Force Field (ReaxFF) is an empirical force field, but its parameters are derived from quantum mechanics calculations [33]. In this force field, in order to realize smooth transitions of bond formation and bond dissociation, the bond energy is determined by bond-orders. In the case of non-bonded potentials, a modified Morse potential function is employed to compute van der Waals interactions, and the Coulomb's law is used to obtain the charge interactions. ReaxFF has already been applied to wide applications, including organic reactions, alkoxysilane gelation, and transition-metal-catalyzed nanotube formation, with good accuracy [33]. In this work, ReaxFF and OPLS potentials were selected to model PE. The detailed information of these two force fields is shown in Appendix A.

2.3.3 Validation of OPLS and reactive force fields

The accuracy of ReaxFF [51] and OPLS to model PE was validated in terms of geometric relaxation of crystal PE; thermal density variations of crystal PE; and phase diagram calculations.

Geometric relaxation of crystal PE: Table 2.1 lists geometric parameters of crystal PE relaxed with the PBE functional and MD simulations with ReaxFF and OPLS at 0 K, along with experimental values [52]. Comparing with experimental and PBE results, it can be concluded that both ReaxFF and OPLS provide an acceptable accuracy to model PE.

Table 2.1: Geometric parameters of crystal PE relaxed with the PBE functional, ReaxFF and OPLS MD simulations at 0 K, together with experimental results [52].

Geometric parameters	PBE	ReaxFF-MD	OPLS-MD	Expt.
a (Å)	6.962	6.982	7.369	7.42±0.01
b (Å)	4.822	4.812	4.916	4.95±0.01
c (Å)	2.560	2.559	2.532	2.55±0.004
$l_{\mathrm{C-C}}$ (Å)	1.528	1.558	1.528±0.001	1.530
$l_{\mathrm{C-H}}$ (Å)	1.102	1.117	1.091±0.001	1.090
$\angle_{\mathrm{C-C-C}}$ (deg.)	113.77	110.407±0.001	111.83±0.01	112±0.3
$\angle_{\mathrm{C-C-H}}$ (deg.)	109.36	110.598±0.020	109.55±0.01	109.5

Thermal density variations of crystal PE: With ReaxFF and OPLS, a 2×2×10 supercell of PE structure was equilibrated by MD simulations at NPT ensemble over 1 ns, where T in a range of 300 – 700 K and pressure at 1 atm. The resulting densities at different T are shown in Fig. 2.4, within 10 % of available experimental values at 300 K [53]. Moreover, it can be observed that the densities obtained from ReaxFF and OPLS based MD simulations decrease sharply at T =

520 K amd 660 K (dashed lines), respectively, which is defined as the melting point T_{m}.

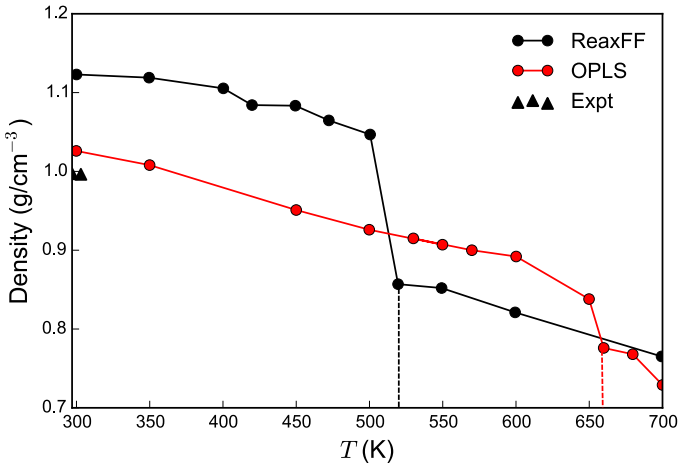

Figure 2.4: Density (g/cm^3) of crystal PE at different temperature (T, in K), obtained from MD simulations with ReaxFF (black circles) and OPLS (red circles) at pressure of 1 atm, together with experimental data from Ref. [53] (denoted by black triangles).

Phase diagram of PE: Following the same method described above, T_{m} of crystal PE at different pressure (i.e., 1, 250, 500, 780, 1000 atm) were predicted. This information was used to generate the phase diagram of PE, as shown in Fig. 2.5, in which T_{m} at different pressures become a boundary between solid and liquid phases. Experimental [54] and computed results with ReaxFF and OPLS are denoted by green, black and red lines, respectively. It can be seen that results obtained from ReaxFF is better than that of OPLS, indicating that it is limited to use the OPLS at the high temperature. More details are provided in Appendix A.3.

2.4 Computational Details

DFT calculations were performed using the Vienna *ab-initio* simulation package (VASP) [55]. Monkhorst-Pack **k**-point meshes [56] used for our calculations are

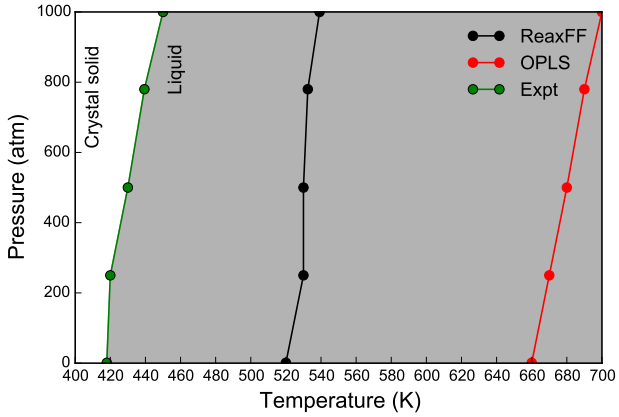

Figure 2.5: Phase diagram of PE with solid and liquid phases denoted by blank and shaded regions, respectively. The black, red and green circle lines are phase boundaries obtained from MD simulations with ReaxFF and OPLS, and experimental values from Ref. [54], respectively.

summarized in Table 2.2. Except kinks and large-scale physical disorders, for which the structures were obtained directly from MD simulations, the structures with other defects/disorder were relaxed using the PBE XC functional [57]. The Tkatchenko-Scheffler functional was used for van der Waals interactions [58]. In calculations involving charged defects, first-order monopole corrections were used to correctly describe the electrostatic interactions of charged defects due to the periodicity and the finite supercell sizes. To obtain the vibrational frequencies of PE, the finite displacement method implemented in the PHONOPY [46] has been used.

Table 2.2: Number of atoms N_{at}, energy cutoff E_{cut}, given in eV, and the k-point meshes used for calculations. More details of models are shown in Table B.1 of Appendix B.

Systems	N_{at}	E_{cut}	k-point
PE unit cell	12	1000	4×4×10
Physical defects (crystal region)	120	400	4×2×2
Large-scale physical disorders	1202*/2402**	400	1×1×1
Chemical defects	68–75	400	4×2×2
Metal/PE interfaces	296–324	400	2×2×1

*Lamella/amorphous region of PE; **Semi-crystalline PE.

Ab-initio MD simulations were performed with VASP, while classical MD simulations were carried out with ReaxFF [33] and OPLS force fields, using the LAMMPS simulation package [59]. A time-step of 0.5 fs was used in the *Ab-initio* and ReaxFF-based MD simulations, while 1 fs was applied in OPLS-based MD simulations. The simulation time of MD simulations involving NPT dynamics was determined to obtain the convergence of densities at each specific temperature and pressure.

Chapter 3

Electronic Structure of Physical Disorder in Polyethylene

3.1 Introduction

Physical disorder refers to morphological, conformational or density deviations from the perfect crystalline PE structure. As shown in Fig. 1.1 (a), bulk PE is composed by crystalline (within lamellas) and amorphous regions, therefore, large-scale morphological imperfections are parts of PE. In addition, because crystalline regions of PE are generated by cooling the molten states [1, 14], physical imperfections, including density variations, branches, cross-links and some conformational disorders, e.g., gauche conformations and kinks, are inevitably present in PE [1, 14]. All these disorders may modify the electronic structure of PE.

This chapter starts with a discussion involving the electronic structure of the perfect crystal PE. Then various physical disorders as mentioned (requiring enormous

unit cells containing up to 2,400 atoms) are constructed and examined, revealing their roles in determining the electronic structure and in manipulating the electronic and carrier transport properties of PE. Such studies are non-trivial, as high-fidelity modeling of polymers in the required large scales is intrinsically challenging [5].

3.2 Perfect Crystal

Crystalline PE has two all-trans CH_2 chains packed in an orthorhombic unit cell, as shown in Fig. 3.1 (a). These chains, characterized by strong intra-chain hybridized sp^3 bonds, are held together by rather weak van der Waals (vdW) interactions. Table 3.1 lists the effect of inclusion the dispersion correction on the lattice parameters of crystal PE. Compared with the experimental values, it indicates that the PBE functional significantly overestimates the lattice parameters of crystal PE, with the mean absolute relative deviations (MAD) being 7.88%. This can be greatly improved by the application of Tkatchenko-Scheffler vdW correction (denoted by PBE-TS) [58], resulting in predicted lattice parameters with a MAD within 3%.

Table 3.1: Lattice parameters of crystal PE with and without vdW corrections, together with mean absolute relative deviations (MAD) with respect to experimental values [52].

Methods	a (Å)	b (Å)	c (Å)	MAD (%)
Expt.	7.42	4.95	2.55	
PBE	8.20	5.60	2.55	7.88
PBE-TS	6.96	4.82	2.56	2.81

The computed band gap of the crystal PE is 8.28 eV with the HSE06 functional, agreeing well with the experimental value of 8.8 eV. Its detailed electronic

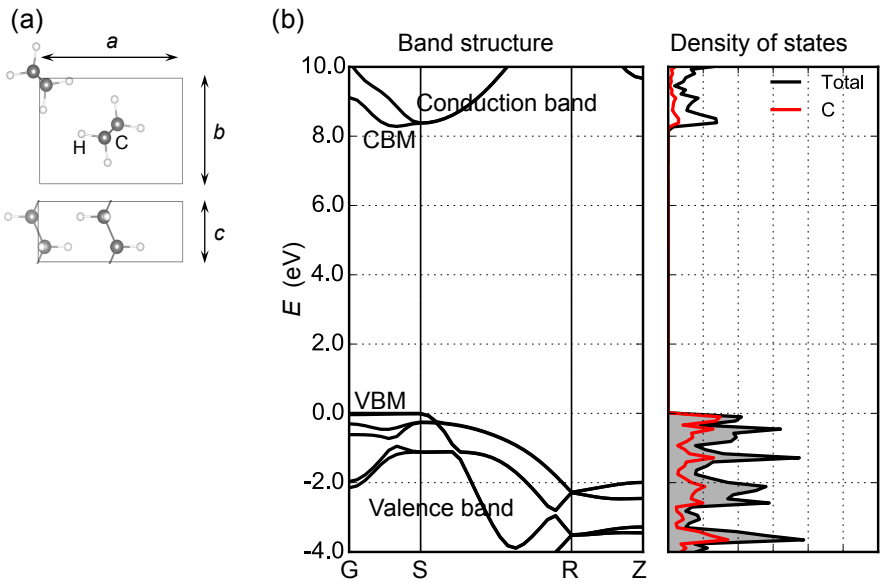

Figure 3.1: Physical (a) and electronic (b) structures of the perfect crystal, along with density of states. *a*, *b*, and *c* are lattice constants of the crystal PE. C and H atoms are grey and white circles, respectively. CBM and VBM are the conduction band minimum and the valence band maximum of PE, respectively.

structure shown in Fig. 3.1 (b), reveals that the VBM of PE is located at the G and S reciprocal space points, dominated by the sp^3-σ bonds associated with intra-chain C atoms. The CBM is located between the G and S points, characterized by hybridized anti-bonding orbitals between adjacent PE chains. Thus, physical or chemical modifications of the chains and/or the distance between them may alter the electronic properties of PE significantly.

3.3 Physical Disorder

In this work, the electronic structure of both large-scale physical disorders and physical imperfections within the crystal regions, including density variations, branches,

cross links between chains, non-uniform bond length and angles (referred to as NU-$l_{\mathrm{AB}}/\angle_{\mathrm{ABC}}$, where A, B, C are atoms), gauche conformations (conf.) and kinks [1,8], were investigated, as shown in Fig. 3.2.

3.3.1 Models

Physical disorders were generated with systems ranging from 120 to 2402 atoms. Disorders in the crystal region were constructed within a $1 \times 2 \times 5$ supercell of crystalline PE, 120 atoms in total. Density variation was captured by changing the inter-chain distance to obtain a density ρ range of $1.03 - 0.36$ g/cm^3 (for perfect crystalline PE, $\rho = 1.08$ g/cm^3). Branches were created by replacing a hydrogen with a $\mathrm{C}_n\mathrm{H}_{2n+1}$ group ($n = 1-4$) while $\mathrm{C}_5\mathrm{H}_8$ chains were used to link PE chains, forming cross links disorders. NU-$l_{\mathrm{AB}}/\angle_{\mathrm{ABC}}$ and gauche conformations were generated via first-principles NVT-MD simulations ($T = 300$ & 700K, respectively) over 1 ps.

In the case of kinks and large-scale disorders, MD simulations with ReaxFF were used. Kinks were generated using NPT-ensemble MD ($P = 1$ atm and $T = 520$ K) over 100 ps, for which the parameters were determined from the phase diagram in Fig. 2.5. A lamella was generated using a multi-step procedure. First, an NVT-MD simulation at $T = 300$K was performed over 200 ps, starting from a supercell containing a folded PE chain of 1,202 atoms. A NPT-MD simulation ($P = 1$ atm & $T = 300$ K) followed, resulting in a reasonable density. Amorphous disorders were generated by simulating the lamella configurations with NVT MD at $T = 600$ K over 100 ps. The temperature of the obtained liquid PE was then

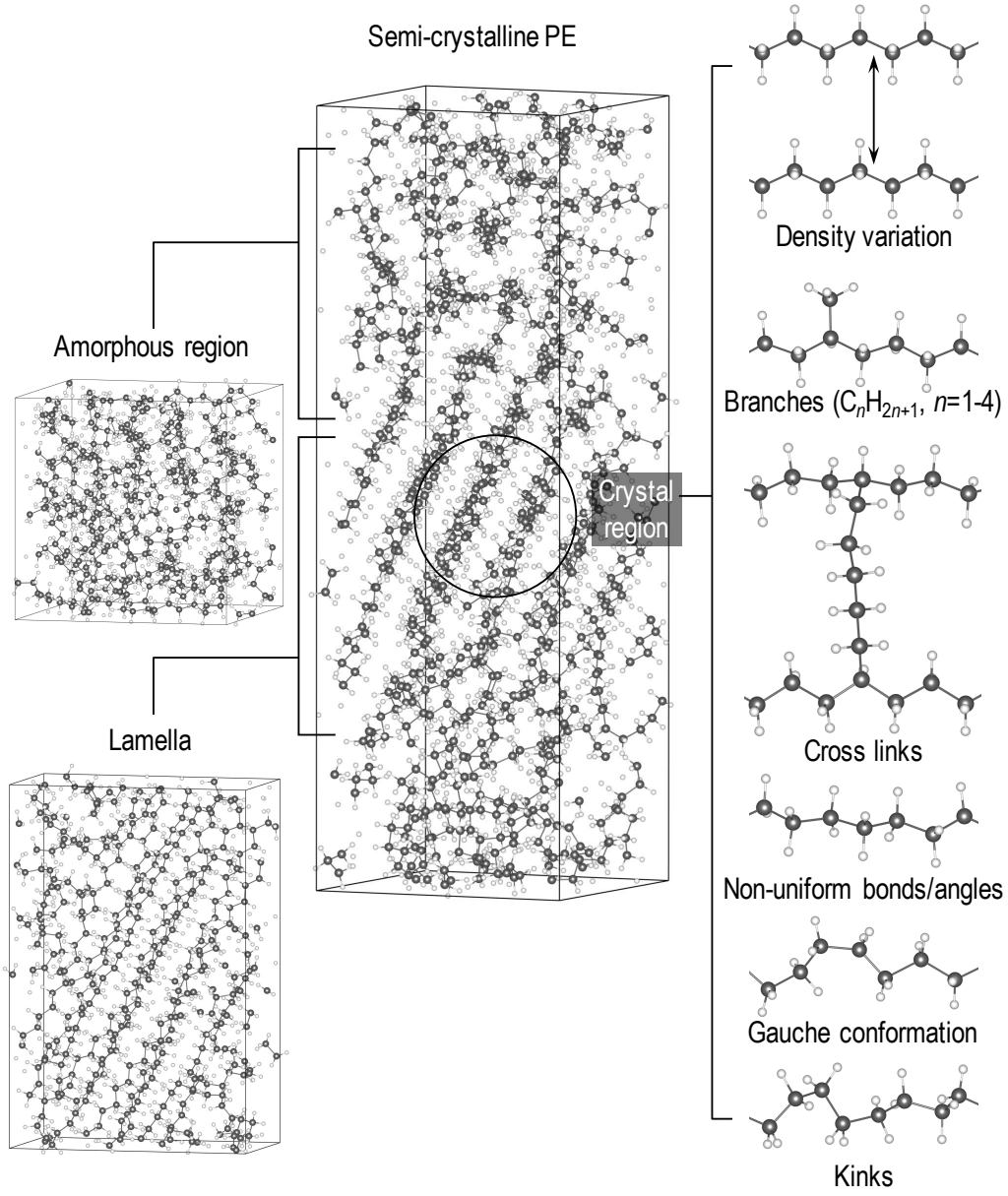

Figure 3.2: Geometries of physical disorders considered: disorders in the crystal region, including density variation, branches, cross links, non-uniform bonds/angles, gauche conformation and kinks; and large-scale disorders, containing pure lamella, amorphous region and semi-crystalline. C and H atoms are grey and white circles, respectively.

lowered to 300 K during the second NVT-MD simulation over 100 ps before the last MD simulation with NPT ensemble (T = 300 K) is carried out for 200 ps. The preparation of semi-crystalline PE structures included two MD simulations performed on a supercell of 2,402 atoms, prepared by combining the lamella and amorphous equilibrium structures. First, an NVT (T = 300 K) MD simulation was performed during 10 ps, and then, an NPT (P = 1 atm & T = 300 K) simulation followed for 400 ps. The resulting density of 0.97 g/cm^3 belongs to HDPE [1]. Except for branches and cross-link disorders, 10 configurations were either generated separately (with different a/b ratio) for density variation or randomly selected from the equilibrated MD trajectories for other disorders.

3.3.2 Kohn-Sham electronic structure

The HSE06 electronic band diagrams computed for PE with these disorders are shown in Fig. 3.3. All energy levels are with respect to the average C-1s core level of the perfect crystal PE whose VBM is set to 0 eV. Error bars of VBM and CBM are obtained by determining the standard deviations from 10 different configurations considered for each disorder/defect. The average computed trap depths, i.e., $E_{\rm t}^{\rm e}$ and $E_{\rm t}^{\rm h}$, are also given in Table 3.2.

Fig. 3.3 shows that when the density ρ varies from 0.36 g/cm^3 to 1.03 g/cm^3, the VBM is essentially the same with that of perfect PE while the CBM is dramatically shifted down. This implies that electrons prefer to transfer from high- to low-ρ regions, as previously indicated [60]. The reason is that in low-ρ PE, the large

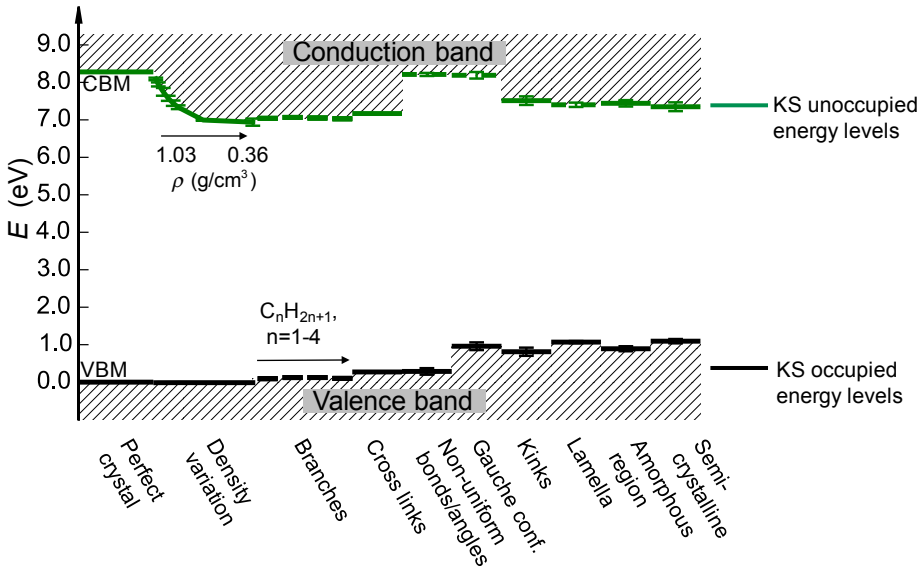

Figure 3.3: Kohn-Sham (KS) electronic structure of physical disorders, computed with the HSE06 functional. Error bars of VBM and CBM are obtained by determining the standard deviations from 10 different configurations considered for each disorder/defect. All energy levels are with respect to the average C-1s core level of the perfect crystal PE whose VBM is set to 0 eV.

inter-chain distance reduces the anti-bonding hybridization, lowering the conduction states. When this distance is large enough (corresponding to $\rho \lesssim 0.54$ g/cm^3), there is essentially no energy difference between the anti-bonding orbitals, thus $E_{\rm t}^{\rm e}$ saturates at $\simeq 1.3$ eV. This value, which is consistent with $E_{\rm t}^{\rm e} \simeq 1.2-1.4$ measured for low-density polyethylene (LDPE) and 1.7 eV measured for HDPE [61], can be ascribed to micro-voids, voids, and cavities of low-ρ PE.

Branches and cross links typically expand the host crystal lattices [66], thus they were constructed in low-ρ PE supercells ($\rho = 0.54$ g/cm^3). With these disorders, ρ is slightly raised, moving up CBM. For branches, the VBM shift of $E_{\rm t}^{\rm h} \simeq 0.1$ eV, originated from the replacement of a $\sigma_{\rm CH}$ bond by a $\sigma_{\rm CC}$ bond, depends weakly on the length of the branches. In the case of cross links, such replacement occurs at both ends of the linking chains, and a deeper $E_{\rm t}^{\rm h} \simeq 0.27$ eV is observed. This

Table 3.2: Computed electron and hole trap depths (E_t^e and E_t^h), given in eV, of PE with physical disorders. Experimental values of E_t^e and E_t^h are given when available. The density ρ of PE (with disorders) is given in g/cm^3.

Configurations			ρ	E_t^e	E_t^h	Expt.
Perfect PE			1.08	0.00	0.00	
Crystal region	Density variation		1.03	0.19	0.00	$1.2-1.4^{\dagger}$ (LDPE) $1.7^{\dagger}$ (HDPE)
			0.98	0.33	0.00	
			0.90	0.53	0.00	
			0.83	0.71	0.00	
			0.77	0.84	0.00	
			0.72	0.94	0.00	
			0.54	1.29	0.00	
			0.36	1.34	0.00	
	Branches	CH_3	0.56	1.24	0.09	$0.24^{\ddagger}$
		C_2H_5	0.57	1.21	0.12	
		C_3H_7	0.58	1.23	0.12	
		C_4H_9	0.60	1.25	0.10	
	Cross links	C_5H_8	0.61	1.11	0.27	
	NU-$l_{AB}/\angle_{ABC}$		1.08	0.07	0.29	$0.32-0.35^{\dagger\ddagger}$
	Gauche conf.		1.08	0.09	0.96	
	Kinks		0.84	0.77	0.81	$1.2^{\ddagger}$
Large-scale disorders	Lamella		0.99	0.88	1.07	–
	Amorphous		0.94	0.84	0.87	$0.8-1.0^{\dagger}$
	Semi-crystalline		0.97	0.93	1.09	$1.0-1.4^{\dagger}$; $1.2^{\ddagger}$; $0.92^{\ddagger}$

† Ref. [61]; ‡ Refs. [62–64]; †‡ Ref. [65]

reveals that the measured E_a of 0.24 eV [63] from transient current is derived from hole-transport induced by branches.

NU-$l_{AB}/\angle_{ABC}$ can reduce the orbital overlaps, ultimately modifying the valence band edges. Bond length elongation diminishes the σ bonding, giving rise to a shallow $E_t^h \simeq 0.29$ eV, being consistent with the trap depth of $\simeq 0.32-0.35$ eV measured for LDPE and HDPE [65]. For the gauche conf., changes in the C–C–C–C torsion angles can dramatically reduce their orbital overlaps, introducing an E_t^h of up to 0.96 eV. An analysis of the projected density of states of kinks, composed of 1 gauche + n all-trans + 1 gauche conformations, reveals that their VBM is

dominated by the gauche part, unraveling the similarity in VBM between kinks and gauche conformations. The resulting $E_t^h \simeq 1.0$ eV, which is consistent with the measured E_a of 1.2 eV for twisting chains [62], suggests that the hole-transport process can be enhanced by the presence of gauche conformations and kinks.

The electronic band diagrams of PE with large-scale disorders, i.e., lamella, amorphous, and semi-crystalline, are portrayed in Fig. 3.2. Similar to gauche conformations and kinks, the VBM of lamella and semi-crystalline PE are attributed to the C–C–C–C torsion angles of $\simeq 60°$ in the folding segments of the PE chains while low-ρ regions are responsible for the drop of the CBM. In semi-crystalline PE, the density of the lamellas/amorphous regions interfaces is very low, thus the CBM is further lowered. We suggest that the low-ρ interface regions play an important role in the conduction of PE because electrons prefer to accumulate here [60]. Different from previous calculations [21], our computed E_t^e of amorphous and lamella/amorphous interface disordered PE are close to the measured trap depths [61]. Moreover, E_t^e computed for semi-crystalline PE agrees well with that experimentally obtained from transient SCLC peak and surface charge decay of HDPE (1.2 eV) and LDPE (0.92 eV) [63, 64].

3.4 Summary

In summary, the role of various physical disorders in determining the electronic structure of PE has been investigated by DFT computations and MD simulations. The computed trap depths agree well with experimental values. These results are

further used to clarify roles of physical disorders in the electric conduction of PE. For example, amorphous and lamella/amorphous interfaces can cause deep electron traps, assisting electron transport between traps and the conduction bands, i.e., trap-controlled band conduction, and enhancing electron conduction. Moreover, kinks, gauche conformations, and folded PE chains can introduce deep hole traps, enhancing the hole transport.

Chapter 4

Electronic Structure of Chemical Defects in Polyethylene

4.1 Introduction

Chemical defects refer to unsaturated bonds, impurities, and possible reaction products [23–25,67]. From the IR-based experimental works [23–25], it is known that unsaturated bonds, e.g., double bond C=C, conjugate double bond C=C–C=C, and vinyl C=CH_2, and oxygen-containing groups, e.g., carbonyl C=O, carboxylate HO–C=O, hydroxyl OH, ether O–C–O, and epoxy-ring C–O–C, are common chemical defects in PE. For halogen doped PE films, additional C-halogen (Cl, Br and I) bonds inevitably exist [64, 67]. In this chapter, the electronic structure of all these defects, as shown in Fig. 4.2, were studied by computing the Kohn-Sham energy levels and thermodynamic/optical charge transition levels. These results can be further used to clarify and confirm the origins of observed luminescence peaks and thermal activation energies [5, 16, 19].

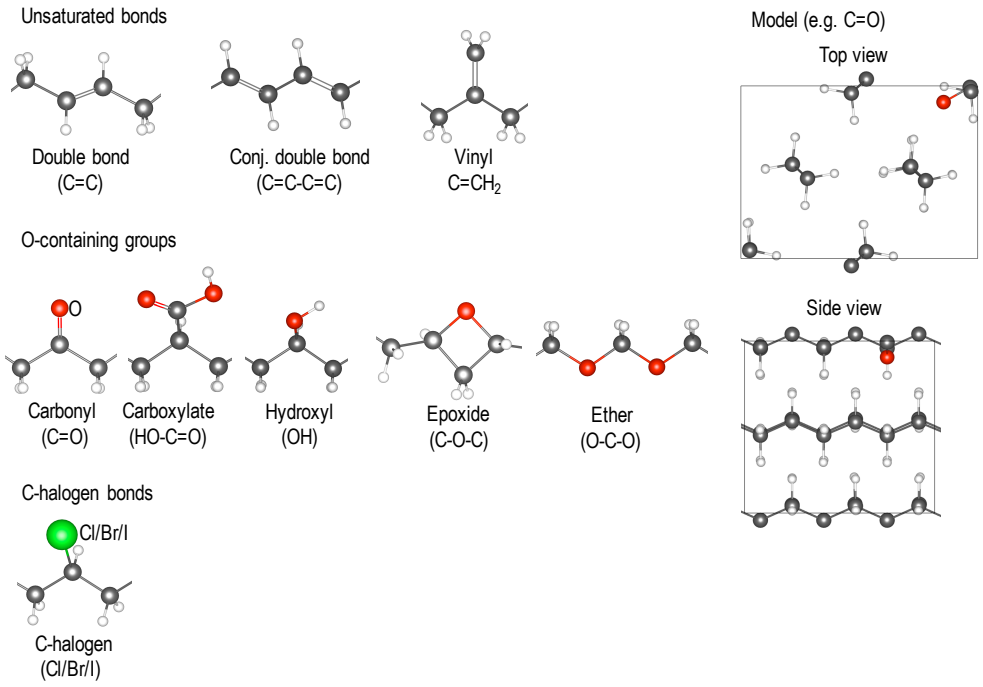

Figure 4.1: Geometries of various chemical defects in PE. C, H, O and halogen atoms are grey, white, red, and green circles, respectively.

4.2 Results and Discussions

4.2.1 Kohn-Sham energy levels

Fig. 4.2 shows the HSE06 electronic structure of PE with various chemical defects. It can be seen that additional occupied and unoccupied energy levels are introduced within the PE band gap. For defects with unsaturated bonds, e.g., C=C, the electron (hole) trapping levels are ascribed to the π bonding (π^* anti-bonding), for which the related p_z orbitals do not align, reducing the overlaps. Among these defects, the electron and hole trap depths, i.e., E_t^e and E_t^h, defined as the shifts of the CBM or VBM induced by defects, of vinyl is largest ($\simeq 3.0$ eV) because its C=C bond locates at the side of the chain.

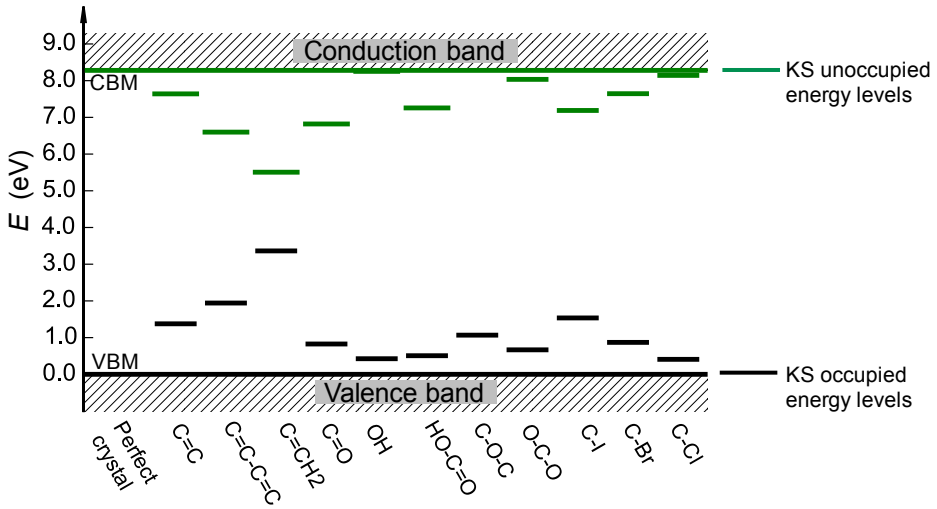

Figure 4.2: Kohn-Sham (KS) defect levels of various chemical defects in PE, computed with the HSE06 functional. All energy levels are with respect to the average C-$1s$ core level of the perfect crystal PE whose VBM is set to 0 eV.

The C=O bond in C=O and HO–C=O defects includes one π_{CO} bond, so the extra electron trapping levels are determined by the energy levels of the π^*_{CO} orbital. In the cases of OH, C–O–C, and O–C–O defects, the only σ^*_{CO} orbital is higher in energy than the σ^*_{CH} orbital due to the same reason. Thus, no or very shallow electron trapping levels were observed in these cases, as can be seen in Fig. 4.2. Unlike unsaturated bond defects, the additional hole trapping levels induced by oxygen-containing groups are determined by the energy levels of the two lone-pair electrons of O, i.e., non-bonding orbitals. The deviations of the hole trapping levels of these defects may be attributed to the difference in their O environment. For instance, the O atom of the C–O–C defect is located at the side chain while for O–C–O defect, O is a part of the backbone.

C–halogen bonds are highly polarizable, thus the $\sigma^*_{\mathrm{C-halogen}}$ orbital is lower than the σ^*_{CH} orbital, leading to additional electron trapping levels. Because the large

Table 4.1: Computed trap depths (E_t^e and E_t^h) and electron and hole activation energies (E_a^e and E_a^h), given in eV, of PE with chemical defects. Experimental values are given when available.

Defects	E_t^e	E_t^h	E_a^e	E_a^h	Expt.
C=C	0.64	1.38	$1.00-1.46$	$0.65-0.84$	
C=C–C=C	1.68	1.94	$1.86-2.06$	$1.13-1.36$	–
$C=CH_2$	2.77	3.36	$1.69-1.81$	$2.96-3.10$	
C=O	1.46	0.83	$1.30-2.17$	$0.34-0.40$	
OH	0.00	0.43	$0.20-0.21$	$0.96-0.97$	1.40 [61]
HO–C=O	1.02	0.51	$0.38-1.36$	$1.93-2.27$	2.0 [63, 64]
C–O–C	0.00	1.07	$0.11-0.30$	$1.06-1.13$	
O–C–O	0.25	0.67	$0.96-2.23$	$0.52-0.57$	
C–I	1.09	1.54	$0.05-0.96$	$2.60-2.70$	0.85 [63, 68]
C–Br	0.64	0.87	$0.60-1.84$	$1.59-1.67$	–
C–Cl	0.14	0.41	$0.55-2.20$	$1.23-1.28$	–

radius of the halogens reduces the C–halogen orbital overlaps, the electron trapping level of C–I bonds is lowest. Similar to O-containing groups, hole trapping levels of C–halogen systems are governed by the non-bonding orbitals of halogens. Computed E_t^e of C–Cl defect is low, presumably because of its strong polarization.

4.2.2 Thermodynamic and optical transition levels

In addition to Kohn-Sham energy levels, thermodynamic and optical transition levels of chemical defects associated with total energy differences of different charged states have been computed with Eqs. (2.2-2.4). These characteristic signatures can be related to measured transport activation energy E_a and luminescences spectra.

The calculated thermodynamic and optical charge transition levels, e.g., $E^{\text{therm}}_{(0/\pm1)}$ and $E^{\text{opt}}_{(0\leftrightarrows\pm1)}$, are shown in Fig. 4.3. The differences between $E^{\text{therm}}_{(0/\pm1)}$ and $E^{\text{opt}}_{(0\leftrightarrows\pm1)}$ are due to the structural relaxation of PE in the vicinity of the defects during charging and discharging. Because $E^{\text{therm}}_{(0/\pm1)}$ and $E^{\text{opt}}_{(0\leftrightarrows\pm1)}$ were computed from the total energy,

they are physically relevant and thus, can be used to unveil the origins of measured activation energy $E_{\rm a}$ and electro- and thermo-luminescences (EL and TL) [5, 19].

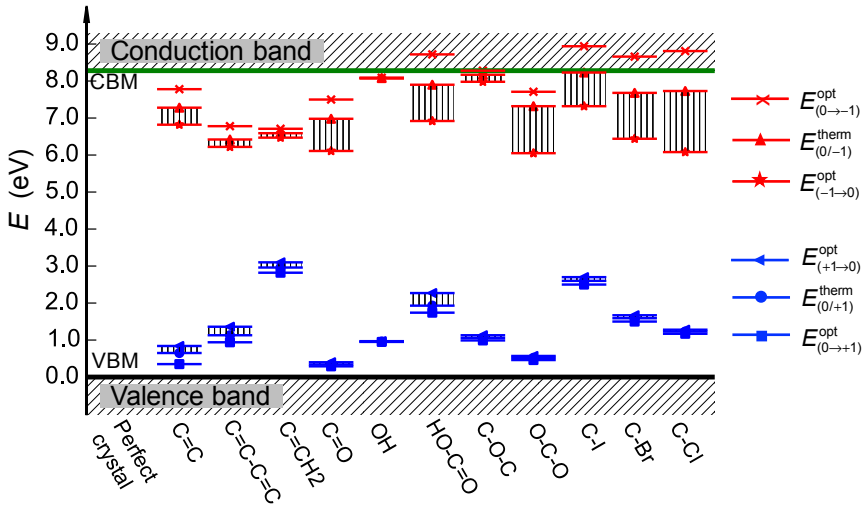

Figure 4.3: $E^{\rm therm}_{(0/\pm1)}$ and $E^{\rm opt}_{(0\leftrightarrows\pm1)}$ are the thermodynamic and optical charge transition levels, respectively. All energy levels are with respect to the average C-1s core level of the perfect crystal PE whose VBM is set to 0 eV.

Measured $E_{\rm a}$ may be associated with energy differences between the band edges and the charge transition levels. By placing the CBM and VBM with respect to $E^{\rm therm}_{(0/\pm1)}$ and $E^{\rm opt}_{(\pm1\leftrightarrows0)}$, the electron and hole activation energies, i.e., $E^{\rm e}_{\rm a}$ and $E^{\rm h}_{\rm a}$, were computed and summarized in Table 4.1. Computed $E^{\rm e}_{\rm a}$ of C=O, HO–C=O and O–C–O agree well with those obtained by X-ray thermally stimulated current experiments (1.4 eV) for oxidation, indicating that C=O and O–C–O may serve as deep electron traps in PE. This claim may also be supported by $E_{\rm a} \simeq 2.0$ eV extracted from mobility measurements of oxidized high-density polyethylene (HDPE) [64]. For PE with C–I bonds, the upper limit of $E^{\rm e}_{\rm a} \simeq 0.96$ eV explains well the origin of measured $E_{\rm a}$ of 0.85 eV for the electronic conduction [63, 68].

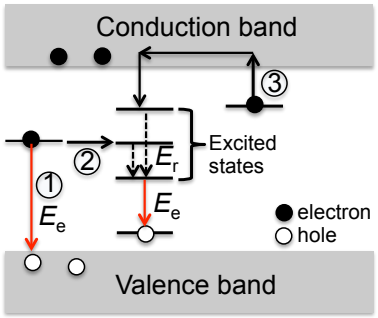

Figure 4.4: Schematic diagram of charge recombination process: ① trapped electron-hole recombination; ② direct tunnelling; and ③ detrapping. E_r is the energy differences of the defect at different excited states.

In addition, energies emitted (E_e) in EL and TL can be related to charge recombinations between different transition levels. The scenario, as sketched in Fig. 4.4, is rather complicated with the involvement of the defect energy levels. The free charges in the conduction band, which were pumped from either the valence band by x-ray or γ-irradiation radiation in TL or the electrodes in EL, may be trapped by (shallow or deep) defect levels. While the trapped electrons can recombine directly with holes in the valence band (① process), those from deep traps can also be transferred to the excited states of the recombination centers by direct tunneling before relaxing to the lowest-excited level for the final recombination (② process). Electrons from shallow traps, on the other hand, can move to the excited states of the recombination centers by going through the conduction band (③ process). It can be seen that to evaluate the emission energies from the charge recombination processes, excited states of neutral chemical defects are required as well. They includes the lowest and higher-energy excited singlet states (S_1 and S_2, respectively), and the excited triplet state T_1.

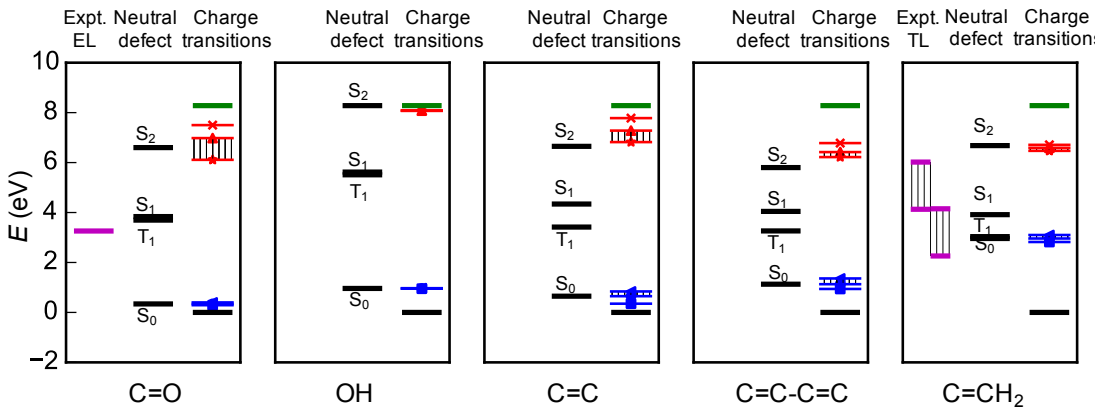

Figure 4.5: Neutral defect ground and excited states (S_0, S_1, S_2, and T_1 states) involved in the intra-defect transitions are shown with black solid lines. The S_0 states are aligned with the $E^{\rm therm}_{(0/+1)}$ levels of defects. The possible transition levels which lead to optical emissions are represented by the shaded region. The experimental EL levels for carbonyl defect is determined by the differences between the $E^{\rm therm}_{(0/+1)}$ and experimental emission energies [27]. While the experiment TL level of vinyl is obtained by the differences between the HSE06 CBM (or VBM) and experimental emission energy [26].

Given the computed defect level placements, excited state energies, and the measured luminescence signatures are portrayed in Fig. 4.5 in a unified manner. Here, only carbonyl, hydroxyl, double bond, conjugated double bond and vinyl defects are considered, due to the limitation of experimental values. We propose that the mechanism ② in Fig. 4.4 underlies the EL spectra of PE containing carbonyl, hydroxyl, double bond and conjugated double bond defects, and that mechanism ① underlies the measured TL spectra of PE containing vinyl defects. More specifically, in the former cases (when we believe mechanism ② is in operation), an electron from the $E^{\rm opt}_{(-1\to 0)}$ of such defects may firstly tunnel to their (energetically well-positioned) S_2 excited state, then pass to the triplet (T_1) excited state by internal conversion and intersystem crossing, and finally transfer to the $E^{\rm opt}_{(+1\to 0)}$ level, accompanied by with emission of photons, i.e., $(\text{defect})^{-1} + (\text{defect})^{+1} \to (\text{defect})^{0}$. The entire process can be represented by $(0/-1) \to S_2 \to S_1 \to T_1 \to (0/+1)$, with the last step leading

Table 4.2: Computed emission energies (E_e, in eV) from charge recombination processes, with available experimental results. The existence of E_e range is because $E^{opt}_{(-1\to0)}$ to $E^{therm}_{(0/-1)}$ or from $E^{opt}_{(+1\to0)}$ to μ(0/+1) are used to compare with experiments.

Defects	Path	E_e	Expt.
C=O	(0/–1) $\to S_2 \to S_1 \to T_1 \xrightarrow{E_e}$ (0/+1)	2.18 – 3.12	2.92[a] (EL)
OH	(0/–1) $\to S_2 \to S_1 \to T_1 \xrightarrow{E_e}$ (0/+1)	3.48	–
C=C–C=C	(0/–1) $\to S_2 \to S_1 \to T_1 \xrightarrow{E_e}$ (0/+1)	1.76 – 2.51	–
C=C	(0/–1) $\to S_2 \to S_1 \to T_1 \xrightarrow{E_e}$ (0/+1)	2.08 – 2.73	–
$C=CH_2$	CBM $\xrightarrow{E_e}$ (0/+1)	5.23 – 5.37	4.13 – 6.02[b] (TL)
	(0/–1) $\xrightarrow{E_e}$ VBM	6.53 – 6.65	

[a]Ref. [27]; [b]Ref. [26]

to the observed EL signature. On the other hand, in the case of the vinyl defect, both $E^{opt}_{(0\to-1)}$ and $E^{opt}_{(+1\to0)}$ are close to the experimental result. This implies that the transition of electrons from the conduction band to the $E^{opt}_{(+1\to0)}$ of vinyl, and electron transferred from $E^{opt}_{(-1\to0)}$ to the valence band, are both likely the origin of the luminescence caused by the vinyl defect. In other words, we use the computed defect charge transition level and excited state placements to arrive at the simplest theory that matches with observations. The proposed recombination pathways, the computed transition/emission energies (at various levels of theory), and available measured EL and TL signatures are listed in Table 4.2.

It is also worth noting a few curious details related to the computed results. Emission energies (E_e) of defects computed with the HSE06 functional are listed in Table 4.2, together with available experimental results. For carbonyl, hydroxyl, double bond and conjugated double bond defects, the emission energy ranges from $E^{opt}_{(-1\to0)} - E^{opt}_{(+1\to0)} - E_r$ to $E^{therm}_{(0/-1)} - E^{therm}_{(0/+1)} - E_r$, where E_r is the energy differences of the fully relaxed defect at S_2 and T_1 excited states, calculated with spinpolarized

HSE06 functional. In the case of vinyl, the emission energy ranges from CBM $-$ $\mu^{\rm opt}_{(+1\to 0)}$ to CBM $-$ $\mu(0/+1)$, or from $\mu^{\rm opt}_{(-1\to 0)}$ $-$ VBM to $\mu(0/-1)$ $-$VBM. We note that the computed emission energies of carbonyl, double bond and vinyl agree well with experimental values.

4.3 Summary

In sum, the electronic structure of chemical defects within PE has been comprehensively investigated, in terms of the Kohn-Sham energy levels and thermodynamic/optical charge transition levels. The former reveals chemical defects (except OH and C–O–C) introduce deep defects states within the band gap, enhancing electron and hole conduction within PE. The latter well unveils the origins of measured activation energy $E_{\rm a}$ and electro- and thermo-luminescences signatures. This computational scheme may be used to interpret the luminescence data of other organic polymers as well. A detailed description of this work is available in Refs. [19] and [69].

Chapter 5

Electronic Structure of Electrode/Polyethylene Interfaces: Charge Injection Barriers

5.1 Introduction

Charge injection at electrode/polymer interfaces in electrical systems is believed to lead to progressive degradation, and ultimately, to the failure of the embedded polymer dielectric layers [8, 12, 70–72]. This process is governed by the electron and hole injection barriers (ϕ_{e} and ϕ_{h}), at the interface [8], defined as the energy difference between the Fermi level and the PE band edges or trap levels, as shown in Fig. 5.1. In principle, charge injection barriers are determined by the appropriate electronic properties of the metal (i.e., its work function), the dielectric (i.e., its band gap and electron affinity), and the interfacial regions (i.e., its dipole moment) [8,12]. In this chapter, the effect of these key factors on the charge injection barriers has been discussed. Moreover, by considering defects/disorders in PE, the computed

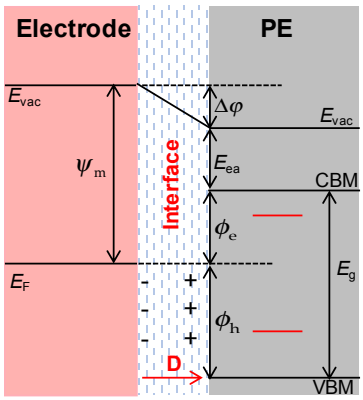

Figure 5.1: Energy diagram of an electrode/PE interface, where E_{F}, E_{vac}, and CBM and VBM are the metal Fermi level, vacuum level, and the conduction band minimum and valence band maximum of PE, respectively. Red lines within the band gap are defects/disorder induced energy states. Due to the interfacial dipole moment $\mathbf{D}$ created after physical contact between the metal and PE, the vacuum levels of the two materials are misaligned by $\Delta\varphi$.

charge injection barriers cover the whole range of the experimental data. These results provide deep insights for understanding the charge injection mechanisms, and can be input variables for building phenomenological transport models in which charge injection barriers are required.

This chapter includes two parts: (1) charge injection barriers of ideal electrode/PE interfaces are discussed, in which the role of metal work function and interfacial dipole moments are highlighted, see Sec. 5.2; (2) more realistic electrode/PE interfaces, via considering oxygen-containing functional groups, have been investigated, where impacts from the presence of defects at interfaces and bulk PE on charge injection barriers are addressed, see Sec. 5.3.

5.2 Charge Injection Barriers of Ideal Electrode/PE Interfaces

In this section, we consider a few metal/PE interfacial configurations in an attempt to span situations encountered in metal/PE systems. As shown in Fig. 5.2, a diverse set of metals (Al, Ag, Au, Pd and Pt) and three different configurations of the PE slab were included, referred to as $PE_{(001)}$, $PE_{(110)}$, and $PE_{(la)}$, wherein the subscript indicates the orientation of the $-CH_2-$ chains of crystalline PE. For $PE_{(001)}$ and $PE_{(110)}$, the $-CH_2-$ chains are normal to and parallel with the metal surface, respectively. PE lamellae, a typical variant of PE whose chains adopt a variety of formats, e.g., curves and fragments [1], is modeled by $PE_{(la)}$ in which these chains are folded, approaching the metal surface from different angles.

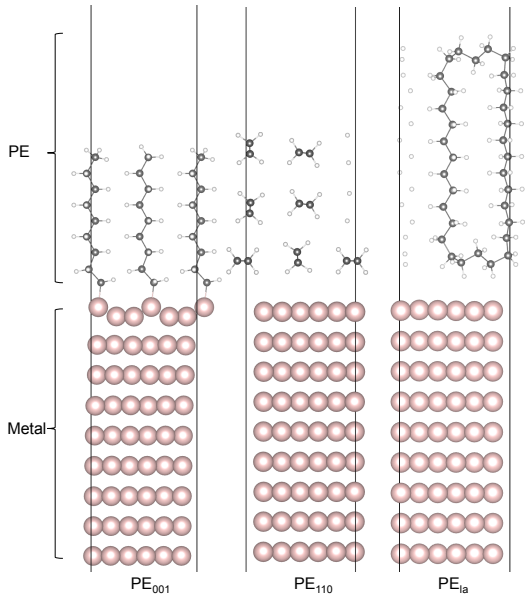

Figure 5.2: Geometries of the metal/PE interfaces considered. Metal, carbon and hydrogen atoms are shown in blue, dark-brown and pink, respectively. PE chains are normal to the metal surface ((a), $PE_{(001)}$), parallel to the surface ((b), $PE_{(110)}$), and are folded next to the surface ((c), $PE_{(la)}$).

From Fig. 5.1, it is known that the essential ingredients necessary to compute $\phi_{\rm e}$ and $\phi_{\rm h}$ for a metal/insulator system include the work function of the metal ($\psi_{\rm m}$), the band gap ($E_{\rm g}$) and the electron affinity ($E_{\rm ea}$) of the insulator, and the interfacial dipole moment-induced vacuum level shift ($\Delta\varphi$). Note that, barring the last quantity (namely, $\Delta\varphi$), the other properties are those of the individual systems that make up the interface. The dipole moment is intimately tied to the interfacial structure and bonding. Below, we present our results for each of these quantities (with the exception of $E_{\rm g}$, which was discussed above), and use them to evaluate the charge injection barriers for the metal/PE interfaces.

5.2.1 The metal work function $\psi_{\rm m}$

The energy needed to remove an electron from a metal, or the work function $\psi_{\rm m}$, can be calculated as the difference between the metal Fermi level and the metal vacuum level. The standard method which has widely been used [**?**] to calculate $\psi_{\rm m}$, referred to as the "bulk plus band lineup" method [73, 74], involves several steps. We show in Table 5.1 the work function calculated for Al, Ag, Au, Pd, and Pt. Calculated results are within 5% of the experimentally measured data, indicating that our DFT-based computational scheme is reasonable for determining $\psi_{\rm m}$.

5.2.2 The PE electron affinity $E_{\rm ea}$

The electron affinity $E_{\rm ea}$ needed in Eq. (2.6) for PE is the energy difference between the vacuum level and the conduction band minimum (CBM) of PE. To determine CBM with respect to the vacuum level, the "bulk plus band lineup"

Table 5.1: Optimized lattice parameters a, b, and c of the orthorhombic $Pnma$ PE crystal and a of the cubic $Fm\overline{3}m$ Ag, Au, Al, Pd, and Pt crystals, all given in Å. The calculated metal work function is given in eV. For validation, relevant experimental data is also provided.

		Lattice constants			Work function		
System		This work	Expt.	Ref.	This work	Expt.	Ref.
PE	a	7.00	7.12	[75]			
	b	4.86	4.85	[75]			
	c	2.56	2.55	[75]			
Al	a	4.05	4.05	[76]	4.05	4.26	[77]
Ag	a	4.15	4.09	[76]	4.43	4.74	[77]
Au	a	4.16	4.08	[76]	5.21	5.31	[77]
Pd	a	3.94	3.89	[78]	5.30	5.60	[77]
Pt	a	3.97	3.92	[76]	5.70	5.93	[77]

procedure described above was used. The electron affinity of the $PE_{(110)}$, $PE_{(la)}$ and $PE_{(001)}$ slabs (with the band edges of bulk PE calculated with G_0W_0 method) are found to be -1.33 eV, -1.23 eV, and -1.16 eV, respectively. These results agree well with the experimentally measured E_{ea} that ranges between -1.20 eV and 0 eV [79].

5.2.3 Interfacial dipole-induced vacuum level shift $\Delta\varphi$

Interfacial effects like charge transfer is ubiquitous in heterostructures, leading to the *interface-originated* vacuum level shift $\Delta\varphi$. Starting from the DFT charge density, the electric dipole $\mathbf{D}$ appearing in Eq. (2.5) was determined by integrating the elementary dipole moment over the whole total volume of the system. Calculated results for the dipole-induced $\Delta\varphi$ are shown in Table 5.2. We note that only the $\Delta\varphi$ of $Al/PE_{(001)}$ takes a positive value, compared with other $metal/PE_{(001)}$ interfaces. This is because the vacuum energy shift is originated from the charge transfer process which is primarily mediated by the metal-carbon bonds formed at the interface. While Al may donate electrons (from the $3s$ and $3p$ shells), the other transition

Table 5.2: Calculated vacuum level shift $\Delta\varphi$ of the metal/PE interfaces, given in eV. Experimental data is taken from Ref. [80] for the metal/TTC interface, which is similar to the metal/$PE_{(110)}$ interface. See text for further details.

System	$PE_{(001)}$	$PE_{(la)}$	$PE_{(110)}$	Expt.
Al-PE	0.29	−0.19	−0.20	−0.30
Ag-PE	−0.20	−0.56	−0.59	−0.50
Au-PE	−1.18	−0.48	−0.58	−0.70
Pd-PE	−1.26	−0.43	−0.72	N/A
Pt-PE	−1.45	−0.59	−0.61	N/A

metals prefer to gain more electrons for closing their d shell. This difference leads to charge transfer, and ultimately, vacuum energy shifts, in opposite directions. To the best of our knowledge, similar data for metal/PE interfaces is unavailable. Therefore, for validation purposes, our results were compared with $\Delta\varphi$ measured for the interfaces between tetratetracontane [TTC - $n CH_3(CH_2)_{42}CH_3$] and Al, Ag and Au [80, 81]. A comparison between the measured metal/TTC and the modeled metal/$PE_{(110)}$ interfaces is justified because their structures are somewhat similar, i.e., the TTC molecules were found to lie parallel to the metal surface [81]. Indeed, the calculated and measured $\Delta\varphi$ are consistent, suggesting that the results of our calculation methodology for $\Delta\varphi$ at the metal/PE interfaces are appropriate for estimating the charge injection barriers using Eqs. (2.6) and (2.7). Nevertheless, we note that the interfacial structure of real metal/PE interfaces may be more complex than the models used here.

5.2.4 Charge injection barriers ϕ_e and ϕ_h

Given the ψ_m, E_{ea}, E_g, and $\Delta\varphi$ calculated by DFT, ϕ_e and ϕ_h were determined and shown Fig. 5.3. The error bars represent the spread in the values due to the choice of the interface geometry.

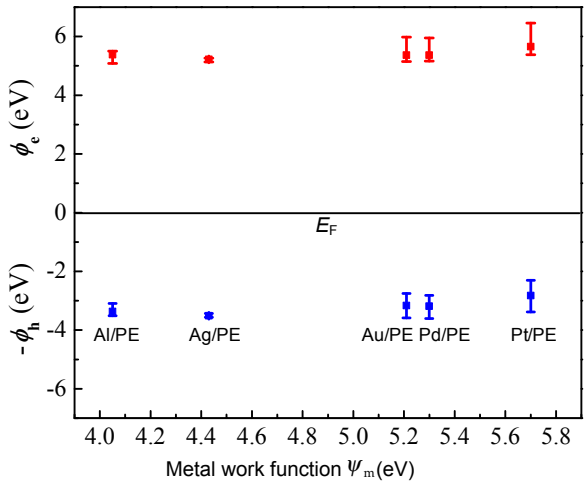

Figure 5.3: ϕ_{e} and ϕ_{h} (denoted by red and blue colors, respectively) of the metal/PE interfaces versus ψ_{m}. The Fermi energy (E_{F}) of all metal is set as 0. The error bars represent the spread in the barrier height values arising from the choice of the interface geometries (based on the data contained in Table 5.2).

It can be seen from Fig. 5.3 that the charge injection barriers do not follow a clear relationship with the metal work function. This aspect is indeed consistent with previous measurements [72]. Furthermore, for a given metal/PE system, the barriers can be significantly modulated by the details of the interface geometry, as captured by the error bars in Fig. 5.3, which further diminishes the variations in the barriers between different metal/PE systems. These observations allow us to appreciate the important role played by the interface; this can potentially outweigh the effects of the metal work function.

In addition, the predicted barriers are only in semi-quantitaive agreement with the limited available measurements (2.14 [82], or 1 eV [12]). The rather partially satisfactory correspondence between computations and measurements for the charge

injection barriers is indicative of the possible difference between the interface model simulated and the real complex situation.

5.3 Charge Injection Barriers of Realistic Electrode/PE Interfaces

In order to predict more accurate charge injection barriers, the effects of Al/PE interfaces with varying amounts of the inevitable O, and of the trap states due to a variety of chemical defects within the band gap, and modulation of the band edge positions due to a plethora of physical and morphological imperfections, were considered in this section.

As shown in Fig. 5.4, we assumed that Al/PE interfaces were fabricated by depositing an Al layer on an oxygen-treated PE film [67, 83], inevitably forming some O-containing groups close to the interface. Al/PE(110) interfaces are selected as a model, because Al is the most common electrode and PE (110) is typical plane in PE. Starting from an ideal (absolutely flat) interface between a PE (110) and an Al slab, two *ab initio* MD simulations were consecutively performed at $T = 300$K and 600K for 1ps. During the MD runs, only the interface region (see Fig. 5.4) was relaxed while the other regions were fixed. The whole Al/PE structure were then optimized using DFT (at 0K) and shown in Fig. 5.4, where the ratio of the carbon atoms to oxygen atoms is 4:1 per layer.

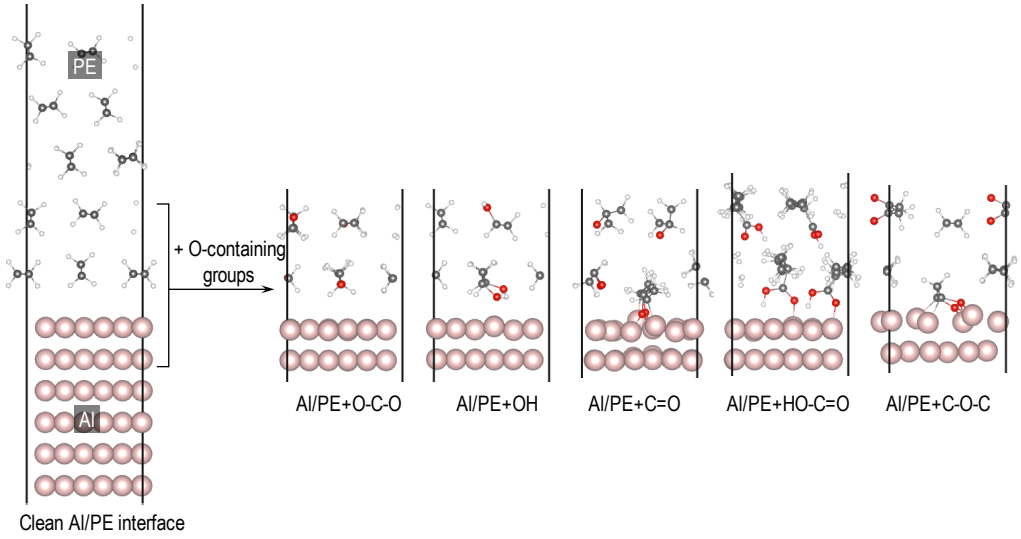

Figure 5.4: Structures of Al/PE interfaces with various O–containing groups, e.g., C=O, O–C–O, OH, HO–C=O, and C–O–C. The Al, C, H, O atoms are pink, grey, white, and red circles, respectively.

5.3.1 Interface structures

In the "clean" Al/PE interface, i.e., that without O-containing defects, PE and Al slabs are separated by $\simeq 3.1$ Å, indicating that only physical interactions exist between the PE and the Al slabs. Due to the large electronegativity of O, the interaction between the Al and the PE+O–C–O slabs becomes stronger, evidenced by a distance of $\simeq 2.6$ Å. For the Al/PE+OH interface, surface Al atoms move toward the PE slab, forming metastable Al–O bonds of $\simeq 2.1$ Å in length. As shown in Fig. 5.2, such Al–O bonds are formed either by breaking a C=O double bond (in the Al/PE+C=O or Al/PE+HO–C=O interfaces), or a C–O bond (in the Al/PE+C–O–C interface). Al–C bonds (of $\simeq 1.8 - 2.0$ Å in length) were also observed in the Al/PE+C–O–C and Al/PE+C=O interfaces. These polarized bonds lead to the work of separation (W) of these two interfaces much greater than other cases, as listed in Table 5.3. Here, W is defined as $W = E_{\mathrm{Al/PE}} - E_{\mathrm{Al}} - E_{\mathrm{PE}}$, in which E

are DFT energies of Al/PE interfaces, pure Al slab and PE slab, respectively. More importantly, these interactions may greatly impact the interfacial dipole moments and hence, the charge injection barriers [22].

Table 5.3: Computed work of separation W (in, J/m^2) and $\Delta\varphi$ (in, eV) of Al/PE interfaces. Data in brackets corresponds to the experimental value.

Interfaces	W	$\Delta\varphi$
Clean Al/PE	0.37	-0.20 (-0.30 [80, 84])
Al/PE+O–C–O	0.71	-1.03 ± 0.53
Al/PE+OH	0.87	-1.38 ± 0.73
Al/PE+HO–C=O	0.91	-1.50 ± 0.27
Al/PE+C–O–C	1.76	-1.56 ± 1.07
Al/PE+C=O	1.82	-1.62 ± 0.70

5.3.2 Interface vacuum energy shift $\Delta\varphi$

Computed $\Delta\varphi$ are summarized in Table 5.3 and Fig. 5.5. For the interfaces considered, $\Delta\varphi$ is negative, signaling a downward shift of the vacuum energy level in the PE side. The increasing trend of $\Delta\varphi$ from Al/PE to Al/PE+O–C–O to Al/PE+OH to Al/PE+HO–C=O and to Al/PE+C=O intuitively indicates the growing strength of $\mathbf{D}$ at the interfaces.

The permanent dipole moments induced by the O-containing groups depend strongly on their orientation. Thus, three positions of such groups in the second layer of the interface region were considered, resulting in a range of calculated $\Delta\varphi$ shown in Fig. 5.5. The most/less negative value of $\Delta\varphi$ was obtained with parallel/anti-parallel O-containing groups in the top two layers. For Al/PE+C–O–C interface, $\Delta\varphi$ can be as large as -2.62 eV while for Al/PE, $\Delta\varphi$ is rather small when the O-containing groups are anti-parallel. Computed $\Delta\varphi$ of Al/PE+O–C–O is larger

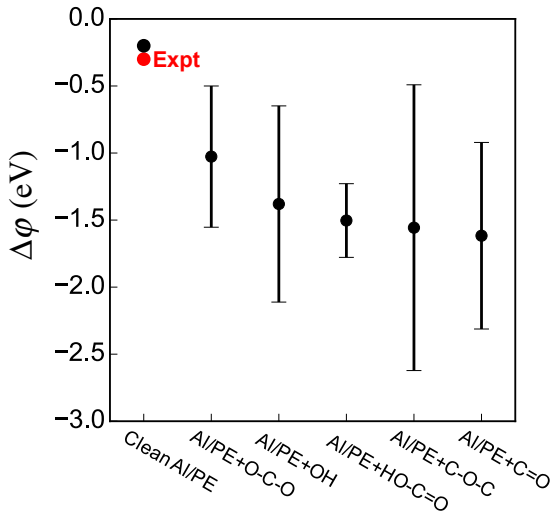

Figure 5.5: Vacuum level shift ($\Delta\varphi$) of Al/PE interfaces with and without O-containing groups.

($\simeq -0.5$ eV) due to the electronegativity of O while for Al/PE+OH, Al/PE+HO–C=O, Al/PE+C–O–C and Al/PE+C=O interfaces, $\Delta\varphi$ is more negative. The reason is that in addition to the permanent dipole moments, Al–O and Al–C bonds also contribute to $\mathbf{D}$ by rearranging the interface charges.

In summary, the primary factors that are responsible for $\mathbf{D}$ and $\Delta\varphi$ are the "pillow effect", the permanent dipole of polar groups, and the formation of polar bonds, of which the last two factors are dominant. Both of them may be introduced by the O-containing groups, significantly dropping the vacuum energy level in the PE side (by $\gtrsim 1.0$ eV) and greatly affecting the charge injection barriers.

5.3.3 Charge injection barriers ϕ_e and ϕ_h

When the bulk region in Fig. 5.4 is perfect, charge injection barriers are energy offsets between the band edges of PE and the Fermi-level of Al. Using Eqs. (2.6)-(2.7), ϕ_e and ϕ_h were computed. Results are listed in Table 5.4 and Fig. 5.6, where E_{et} and E_{ht} are 0 eV for the perfect crystal.

Fig. 5.6 shows, for the perfect crystal case, interfaces including O-containing groups (colorful lines) have a lower ϕ_e, compared to the clean Al/PE interface (black line). An opposite behavior is observed for ϕ_h, because of $\phi_e+\phi_h=E_g$. For instance, the ϕ_e is decreased to 2.69 eV from 4.11 eV for the Al/PE+C=O interface. These observations not only unravel the key of interfacial dipole moments in determining charge injection barriers, but also show that the presence of O-containing groups significantly decrease the ϕ_e value. As a result, the computed ϕ_e ranging from 2.69 – 3.28 eV, fairly agrees with a measured barrier height of 2.14 eV by Taylor *et al* in 1971 [82]. However, predicted values, especially ϕ_h, are still overestimated, compared with recent measurements for a variety of metal electrodes with charge injection barriers of about 1 eV [12]. These discrepancies may be caused by physical and chemical defects within bulk PE because they can provide trapping states for

Table 5.4: Computed ϕ_e, and ϕ_h of Al/PE interfaces, given in eV.

Interfaces	Bulk region of PE					
Configurations	Perfect crystal		Physical defects		Chemical defects	
	ϕ_e	ϕ_h	ϕ_e	ϕ_h	ϕ_e	ϕ_h
Clean Al/PE	4.11	4.17	$2.77-4.04$	$3.08-4.17$	$1.34-4.11$	$0.81-3.66$
Al/PE+O–C–O	3.28	5.00	$1.94-3.21$	$3.91-5.00$	$0.51-3.32$	$1.63-4.49$
Al/PE+OH	2.93	5.35	$1.59-2.86$	$4.26-5.35$	$0.16-2.96$	$1.99-4.84$
Al/PE+HO–C=O	2.81	5.47	$1.47-2.73$	$4.38-5.47$	$0.03-2.84$	$2.11-4.97$
Al/PE+C–O–C	2.75	5.53	$1.41-2.68$	$4.44-5.53$	$0.00-2.79$	$2.16-5.02$
Al/PE+C=O	2.69	5.59	$1.35-2.62$	$4.50-5.59$	$0.00-2.73$	$2.22-5.08$

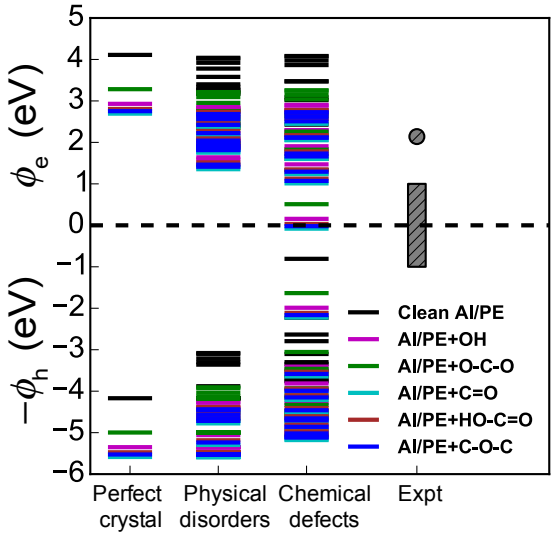

Figure 5.6: Corresponding ϕ_e and ϕ_h for the bulk PE composed by the perfect crystal, physical disorders and chemical defects, along with experimental values [12, 82].

the injected charges, leading to lower charge injection barriers, or deviations of simulated interface models from the real interface.

In order to identify the role of defects in the bulk region of PE, ϕ_e and ϕ_h were estimated by combining with E_{et} and E_{ht} obtained from the "Bulk PE" section. Computed results are summarized in Table 5.4 and portrayed in Fig. 5.6 (b). A range of values for each interface is provided due to a variety of defects. It can be seen that both ϕ_e and ϕ_h are reduced. For example, when physical defects in the bulk region are considered, the ϕ_e can be decreased to 1.35 eV and the ϕ_h can drop to 3.08 eV. This fact highlights the key role played by defects in determining charge injection barriers, since negative $\Delta\varphi$ induced by interfacial dipole moments can increases ϕ_h (or ϕ_e for positive $\Delta\varphi$). In addition, Fig. 5.6 (b) shows that both the resulting ϕ_e and ϕ_h are within the recent experimental value of 1 eV, with considering chemical defects in the bulk region of PE. This is due to deep trap

depths introduced by chemical defects. Furthermore, barrier heights closing to 0 eV are obtained when the *vinyl* defect presents, validating the existence of trap-assisted tunneling mechanism at Al/PE interfaces.

5.4 Summary

An attempt has been made to understand the role of various electronic, physical and chemical factors in controlling the charge (electron or hole) injection barriers at electrode/PE interfaces, via DFT calculations. A variety of metals including Al, Ag, Au, Pd and Pt, and "realistic" metal/PE interfacial models including various oxygen-containing groups were considered. The main conclusions are as follow:

- Charge injection barriers weakly depend on the metal work function, but are affected greatly by the vacuum energy shift determined by interfacial dipole moments, and by trap depths induced by defects/disorder in bulk PE.

- By combining with energy states induced by defects/disorder, the computed charge injection barriers well cover the available experimental values derived from current-voltage measurements.

- When deep energy levels are introduced within the electronic structure of PE, the resulting barrier heights are close to 0 eV. This supports the existence of the trap-assisted tunneling mechanism at Al/PE interfaces, in addition to the Schottky injection mechanism.

Chapter 6

Recap of Electronic Structure Calculations

A *comprehensive* study on the electronic structure of realistic PE, inclusive of a variety of chemical, physical, interfacial and morphological imperfections and disorders (requiring enormous unit cells containing up to 2,400 atoms), has been performed using beyond-DFT calculations and classical MD simulations. Fig. 6.1 shows a summary of our main findings in one unified portrayal, created using one common energy reference. The effect of the interface with Al (containing varying amounts of the inevitable O) on the charge injection barriers, the trap states due to a variety of chemical defects within the band gap, and modulation of the band edge positions due to a plethora of physical and morphological imperfections can all be clearly seen. Main findings and implications are summarized as follows.

1. The role of physico-chemical complexity in determining the electronic structure has been identified.

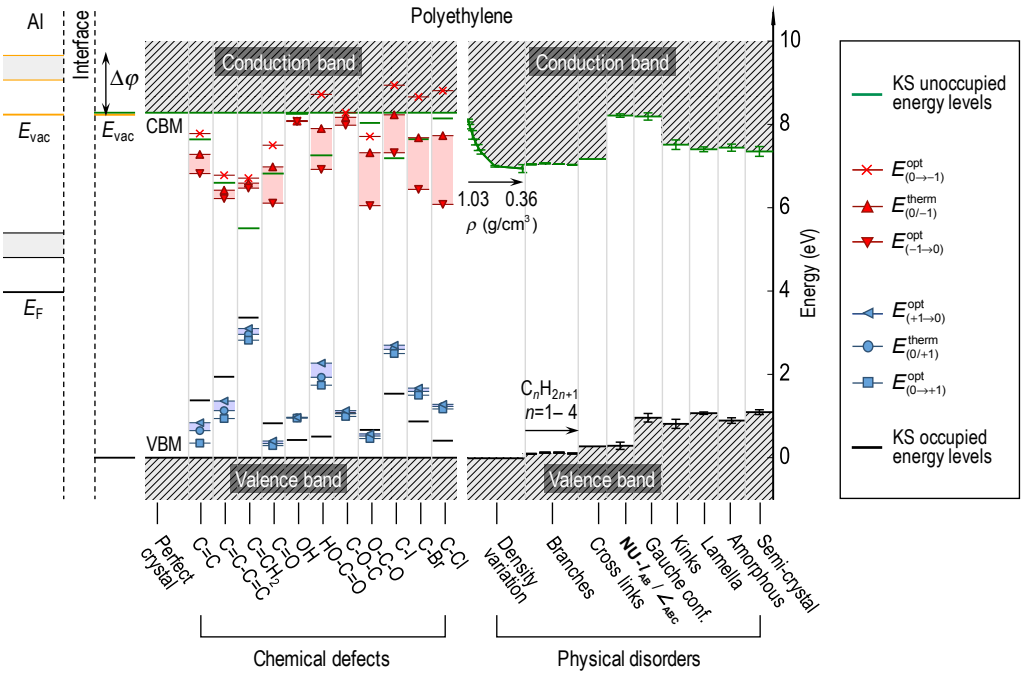

Figure 6.1: Electronic structures of Al/PE interfaces and bulk PE with imperfections. $E_{\rm vac}$, $\Delta\varphi$, $E_{\rm F}$, CBM and VBM are the vacuum level, the vacuum energy shift, the Fermi level of Al, and the conduction band minimum and the valence band maximum of PE, respectively. Error bars of VBM and CBM are obtained by determining the standard deviations from 10 different configurations considered for each disorder/defect. Shaded region of $E_{\rm vac}$ is induced by the O-containing groups at Al/PE interfaces. $E^{\rm therm}_{(0/\pm1)}$ and $E^{\rm opt}_{(0\leftrightarrows\pm1)}$ are the thermodynamic and optical charge transition levels. All energy levels are with respect to the average C-1s core level of the perfect crystal PE whose VBM is set to 0 eV.

2. The proposed computational approach has reached an excellent level of accuracy in determining defect levels, activation energies, trap depths of PE, and the charge injection barriers at the interface between PE and Al electrodes.

3. The obtained electronic structure provides a basis to better understand the existing experimental data involving thermal activation energies, luminescence characteristics and charge injection barriers, the electron/hole transport within PE and across the electrode/PE interfaces, and thus, the long-term degradation of PE.

4. Reported results can be input variables for building phenomenological transport models in which the densities and trap depths of various defects and charge injection barriers are required.

Overall, the key findings of electronic structure calculations, which include not only the numerical results but also the insights into relevant physical and chemical processes, could take us a step closer to understand the polymer degradation in terms of electronic properties. Next, I will move to discuss the relationship between physico-chemical structures and the vibrational behavior of PE that may impact the heat transport in PE.

Chapter 7

Vibrational Behavior of Polyethylene

7.1 Introduction

For polymers, vibrations are the main way to transfer thermal energy. Physical disorders and chemical defects in PE may introduce new vibrational frequencies. Such additional vibrational modes can slow the heat transport by phonon scattering or trapping, which can result in the formation of "hot spots" due to the heat accumulation in local regions. Therefore, it is critical to know the specific effect of various defects/disorders on vibrational frequencies of PE.

In this chapter, the vibrational density of states (DOS) of the crystalline, physical disorders and chemical defects in PE and their implications on the heat transport will be discussed in order. In the case of large-scale physical disorders, e.g., pure amorphous regions, lamellas, and the whole semi-crystalline, MD simulations with OPLS force field have been used to estimate the vibrational DOS. While vibrational frequencies of remaining systems were computed with the finite displacement method

(FDM) implemented in PHONOPY [46]. The computed vibrational frequencies are compared with the available IR experimental data, and further used to estimate their effects on the specific heat capacity.

7.2 Perfect Crystal

The computed phonon band structure and DOS of the perfect crystal PE are shown in Fig. 7.1. The corresponding vibrational frequencies at G point are summarized in Table 7.1, along with other's DFT and experimental values obtained from Ref. [85]. Only 3N-3 (N=12) modes were reported, as the remaining three acoustic modes display negative frequencies owning to the numerical noise. The origins of specific frequency regions are also provided in Table 7.1.

Several observations can be obtained from Fig. 7.1 and Table 7.1. First, the DFT results agree well with experiments, indicating the methodology applied is accurate. Second, phonon vibrations of the perfect crystal, called "bulk" vibrations are determined by C–C and C–H bonds, especially the C–H bonds. Third, the vdw forces between PE chains weakly change the vibrational frequencies, evidenced by little change of frequencies between PE chains (i.e., G to S points in Fig. 7.1). Thus, unlike the electronic structure, only physical or chemical modifications of PE chains may alter the vibrational frequencies of PE.

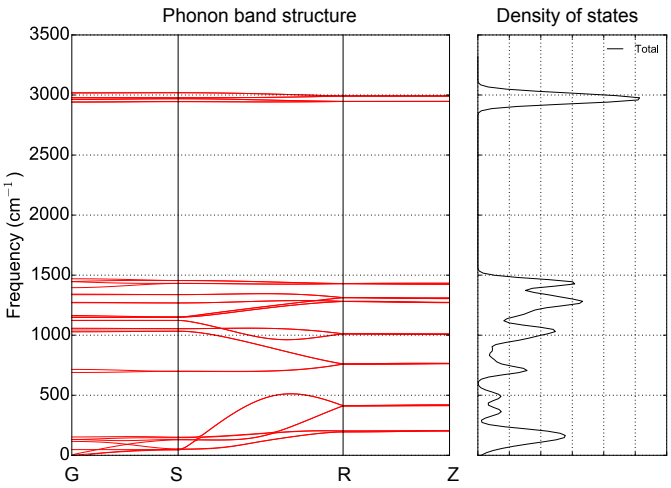

Figure 7.1: Phonon band structure of the perfect crystal, along with density of states.

7.3 Physical Disorder

Next, we move on to discuss impact of large-scale physical disorders including amorphous regions, lamellas, and semi-crystal PE, and disorders in the crystal regions, e.g., the low density with 0.54 g/cm^3, gauche conformations, non-uniform bonds/angles, branches, cross links and kinks, on the vibrational frequencies of PE. In the case of large-scale disorders, the vibrational frequencies were computed using the fourier transform of the velocity autocorrelation derived from MD simulations, since it is more time-consuming using DFT calculations. In this part, OPLS force field were applied instead of the ReaxFF, because OPLS can capture more accurate harmonic forces at the low temperature. The resulting vibrational DOS of large-scale physical disorders are shown in Fig. 7.2. In order to validate the accuracy of OPLS force field, the computed results for the crystal PE are also present in Fig. 7.2. In these MD simulations, there are 2,400, 2,404, 2,404 and 4,804 atoms for

Table 7.1: Computed vibrational frequencies (ω) at Γ point, along with other's DFT and experimental results [85]. Unit: cm^{-1}.

Modes	DFT		Expt.	
	this work	Other's work	Results	Origins
1	47	32	53	–
2	116	74	80	
3	131	97	109	
4	133	104	109	
5	153	114	136	
6	690	708	722	long-chain CH_2 rock
7	715	719	735	
8	1027	748	1057	C-C stretch,bend
9	1034	824	1040	
10	1052	898	1062	
11	1058	917	1050	
12	1123	1025	1180	
13	1124	1041	1187	
14	1148	1058	1173	
15	1150	1116	1134	
16	1150	1136	1114	
17	1164	1169	1172	
18	1270	1185	1296	CH_2 rock
19	1273	1206	1295	
20	1337	1293	1346	CH_2 bend
21	1342	1351	1412	
22	1396	1436	1442	
23	1445	1472	1468	
24	1447	1486	1468	
25	1470	1500	1475	
26	2940	2071	2856	CH_2 symmetric and asymmetric stretches
27	2943	2081	2837	
28	2962	2106	2865	
29	2965	2141	2890	
30	2977	2842	2846	
31	2978	2855	2881	
32	3016	2866	2850	
33	3019	2897	2920	

the crystal structure, pure amorphous regions, pure lamellas, and semi-crystal PE systems, respectively.

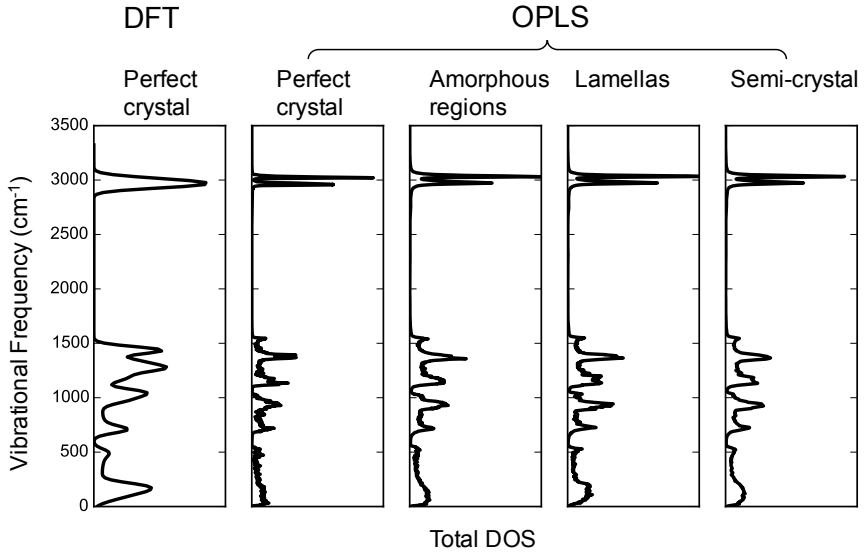

Figure 7.2: Vibrational DOS of the perfect crystal and large-scale physical disorders of PE, computed by DFT calculations with the FDM method or OPLS-based MD simulations

Fig. 7.2 shows the computed vibrational frequencies (ω) of the perfect crystal by OPLS agree well with the DFT results. Moreover, it can be noticed that large-scale disorders only introduce delocalized ω. Such vibrational modes weakly modify the vibrational spectra. In order to further characterize the effect of local morphological imperfections on vibrational ω, FDM method was used to compute the ω of physical disorders in the crystal regions. Their local DOS with the Gaussian distribution is estimated by Eqs. (2.8–2.9).

Fig. 7.3 presents the computed local DOS of physical disorders in the crystal regions, together with their physical structures. It can be seen that because physical structures of defects including the low density with 0.54 g/cm^{-3}, gauche conformations and non-uniform bonds/angles return to the harmonic states, their DOS is the

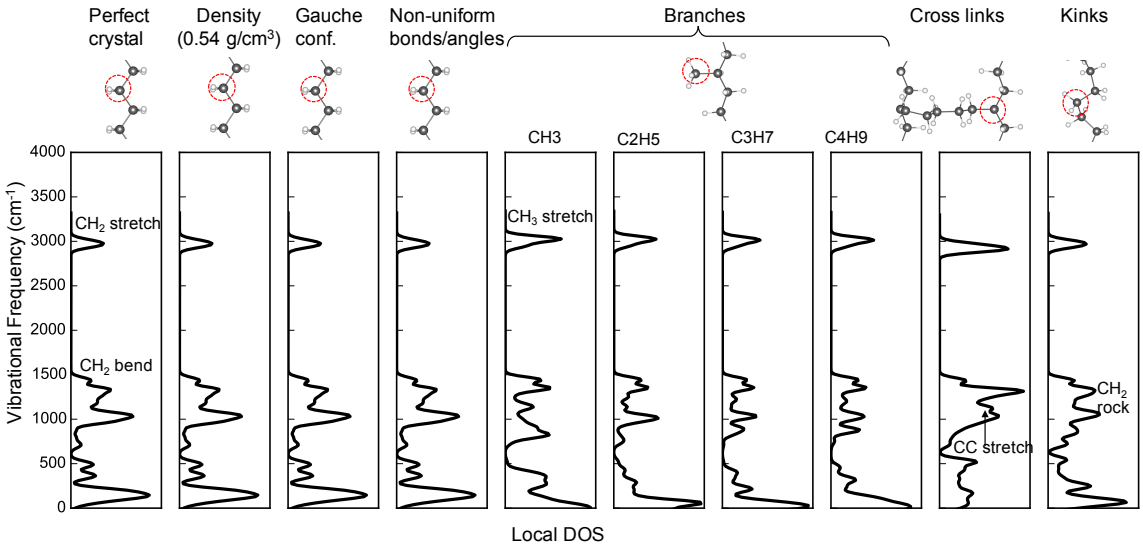

Figure 7.3: Local DOS of physical disorders including the low density with 0.54 g/cm^3, gauche conformations, non-uniform bonds/angles, branches, cross links and kinks, computed with the FDM method. Red circles represent the σ in Eq. (2.9), with a value of 0.5 Å.

same as that of the perfect crystal. We note that the CH_3 ending group in branches induces a little higher C–H stretching ω, i.e., 3026 cm^{-1}, compared with the CH_2 groups ($<$ 3000 cm^{-1}). In the cross links defect, a H is replaced by a CH_2 group, slightly impacting the C–C bond stretching frequencies, as shown in Fig. 7.3. In the case of kinks, its various C–C–C–C torsion angles may affect the CH_2 rocking frequencies, resulting in a new ω of 1325 cm^{-1} observed from Fig. 7.3. This is within the experimental results in a range of 1300 – 1400 cm^{-1} [14]. While these results suggest that local physical disorders indeed alter the vibrational DOS, but they do not introduce additional frequencies, making it difficult to be identified by experiments.

7.4 Chemical Defects

Finally, we attempt to investigate the impact of chemical defects in PE on the vibrational behavior. The local DOS of chemical defects as computed using Eqs. (2.8–2.9) are shown in Fig. 7.4. It can be seen that additional vibrational frequencies are indeed introduced by chemical defects. The corresponding stretching vibrational frequencies are summarized in Table 7.2, along with bond lengths of chemical defects and available experimental values [14, 28]. It shows that computed stretching vibrational frequencies agree well with experimental results.

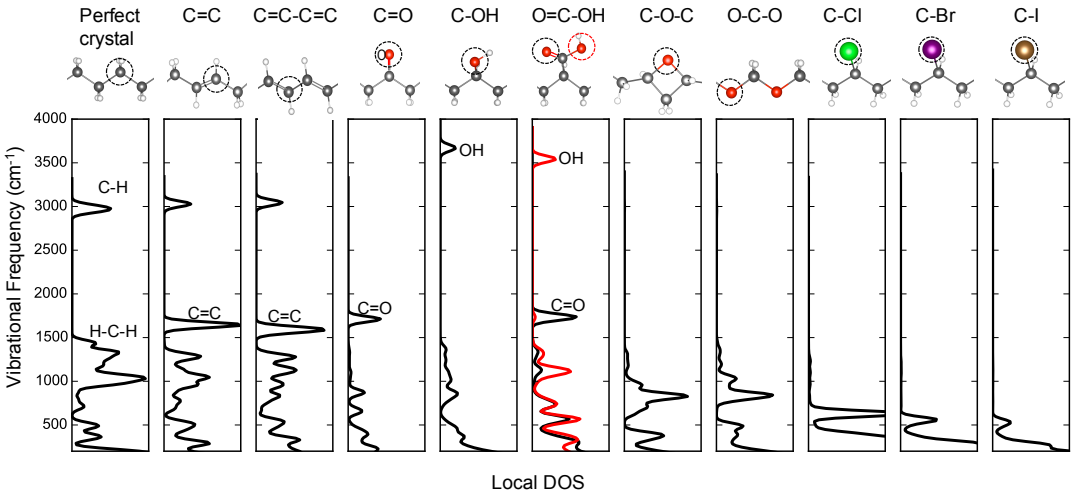

Figure 7.4: Local vibrational DOS of various chemical defects. Black and red circles represent the σ in Eq. 2.9, with a value of 0.5 Å.

Analysis of Table 7.2 and Fig. 7.4. shows that C–halogen bond stretches introduce very low vibrational frequencies ranging from 520 – 633 cm^{-1}. This is because their weaker bond strength compared with the C–C bond, evidenced by their larger bond lengths observed. In the cases of C–O–C and O–C–O defects, C–O bond stretching and C–O–C bending introduce ω at 1200 – 1300 and 800 – 900 cm^{-1},

Table 7.2: Computed bond length and vibrational frequencies (ω) of chemical defects, along with available IR results [14, 28].

Systems	Bond length (Å)		Stretching ω (cm^{-1})	
			Calculated	Expt.
Perfect crystal	C–C	1.528	1000–1200	800–1200
	C–H	1.102	2837–2920	2800–3000
C=C	C=C	1.344	1638	1630–1680
C=C–C=C	C=C	1.360	1583	
C=O	C=O	1.228	1714	1720
OH	OH	0.974	3663	3371
O=C–OH	C=O	1.222	1739	1713
	OH	0.982	3536	–
C–O–C	C–O	1.507	1200–1300	–
O–C–O	O–C	1.466	1200–1300	–
C–Cl	C–Cl	1.797	633	750
C–Br	C–Br	1.965	566	600
C–I	C–I	2.15	520	500

respectively. However, such frequencies overlap with that of C–C bonds, as can be seen in Fig. 7.4. Thus, such frequencies are difficult to be captured by experiments.

For defects involving double bonds, e.g., C=C, C=C–C=C, C=O, and O=C-OH, one additional π bond is included, resulting in stronger bonds and thereby higher vibrational frequencies in a range of 1583 – 1740 cm^{-1} as observed. The OH bond in the OH and HO–C=O defects induces high vibrational frequencies (3500 – 3700 cm^{-1}), due to the strong σ_{OH} bond.

In addition, several inferences can be drawn from Table 7.2. First, the stretching ω follow $\omega_{C-H} > \omega_{C-C} > \omega_{C-O} > \omega_{C-Cl} > \omega_{C-Br} > \omega_{C-I}$, revealing that ω_{C-X} single bonds decrease with an increase in the atomic mass of the X atom. However, this is at variance with the defects including double bonds. For example, vibrational frequencies of C=C is lower than that of C=O, due to the high electron negativity of O atoms and thereby greater bond energies for π bonds. Second, in a group of bonds between the same atoms, the vibrational frequencies increase with the bond

orders, e.g., $\omega_{\mathrm{C-C}} < \omega_{\mathrm{C=C}}$ and $\omega_{\mathrm{C-O}} < \omega_{\mathrm{C=O}}$. Finally, defects made by jointing the same or different defects have lower ω than individual defects, for instance, $\omega_{\mathrm{C=C-C=C}} < \omega_{\mathrm{C=C}}$.

These findings suggest that the stretching vibrational frequencies are determined by the bond energies. In other words, vibrational frequencies can be used to estimate the probability of the specific bond breakage in the degradation. For example, C=O and C=C are more likely to be broken, compared to the OH. Therefore, these two defects can be potential "initial points" of the chemical degradation in PE.

7.5 Implications on Heat Transport within PE

According to discussions above, physical disorders and chemical defects introduce delocalized and localized vibrational modes, respectively. These modes may impact the heat transport within PE in terms of the specific heat capacity (C) and the thermal conductivity (k).

The specific heat capacity (C) corresponds to the amount of thermal energy required to raise the temperature of 1 mole of the system by 1 K. In this part, we focus on the heat capacity at constant volume (C_{V}). Fig. 7.5 (a) shows the C_{V} of the perfect crystal computed by DFT and MD simulations with the OPLS force field, agreeing well with the experimental heat capacities at constant pressure (C_p) [86]. This is because PE is in a solid state at the low temperature (<400 K), where the C_p and C_{V} are close.

From Fig. 7.5 (a), we also note that large-scale physical disorders, e.g., lamellas and semi-crystal PE lead to little deviations in C_{V}. In the case of amorphous regions of PE, the computed C_{V} is consistent with the experimental C_p (denoted by pink circles in Fig. 7.5 (a)) at the low temperature ($T < 150$ K). The large deviations at the high temperature (T $>$ 200 K) may be caused either by the difference between C_p and C_V for amorphous PE, or by the limitation of the OPLS force field used. These results indicate that large-scale disorders only slightly change the C_V due to their weak impact on the vibrational spectra (see Fig. 7.2). We next move to identify the impact from chemical defects on vibrational frequencies and thus on the C_V, as shown in Fig. 7.5 (b). We note that although little change of C_V observed at $T < 100$ K, an increase about 2–4 J/K/mol in C_V is indeed observed for chemical defects at the high temperature, due to additional vibrational frequencies introduced. Based on the results above, in general, it can be concluded that physical disorders and chemical defects in PE modify the C_V weakly.

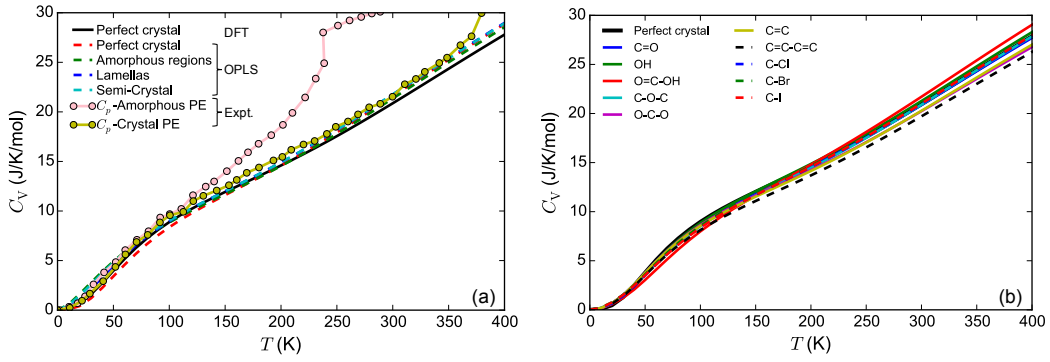

Figure 7.5: (a) Heat capacities (C_{V}, in J/K/mol) vs temperature (T, in K) of the perfect crystal and large-scale physical disorders, along with available experimental C_p values [86]. (b) C_{V} vs T of local chemical defects, computed by DFT.

Unlike the specific heat capacity, the thermal conductivity (k), defined by $\frac{1}{3}C_{\mathrm{V}}l$ where l is the mean free path, are greatly affected by physical disorders and chemical defects. This is because physical disorders and chemical defects can enhance the phonon scattering, leading to a decrease of l and hence k. As a result, the heat transport within polymers will be blocked, causing local overheating that can lead to irreversible polymer damages. This issue will be addressed in the future.

7.6 Summary

In this chapter, a complete picture of the vibrational density of states of "real" PE has been presented, including various physical disorders and chemical defects. Using either MD simulations with OPLS force field or DFT calculations with FDM, the computed vibrational frequencies agree well with experimental values. These results show that physical disorders and chemical defects introduce delocalized and localized vibrational frequencies, respectively. Although such frequencies were found to weakly impact the specific heat capacity of PE, they are expected to substantially decrease the thermal conductivity by scattering phonons. These results provide insights toward understanding the heat transport within PE.

Chapter 8

Summary, Impacts and Future Work

8.1 Summary

In this research, I systematically studied the relationships between physico-chemical structures and the relevant properties (i.e., the electronic structure and vibrational behaviors) of "realistic" PE via computations, as shown in Fig. 8.1. This information is the key gateway towards understanding the electrical degradation phenomena. Because realistic polymers comprise of exceedingly complicated interface morphologies and multi-scale chemical defects and physical disorders, properly modeling them in a consistent level of theory is challenging and has not been previously performed thoroughly. The main findings of this research are summarized as follows:

1. Electronic structure of PE:

   A comprehensive picture of the electronic structure of realistic PE has been presented, systematically examining a majority of inevitable imperfections in

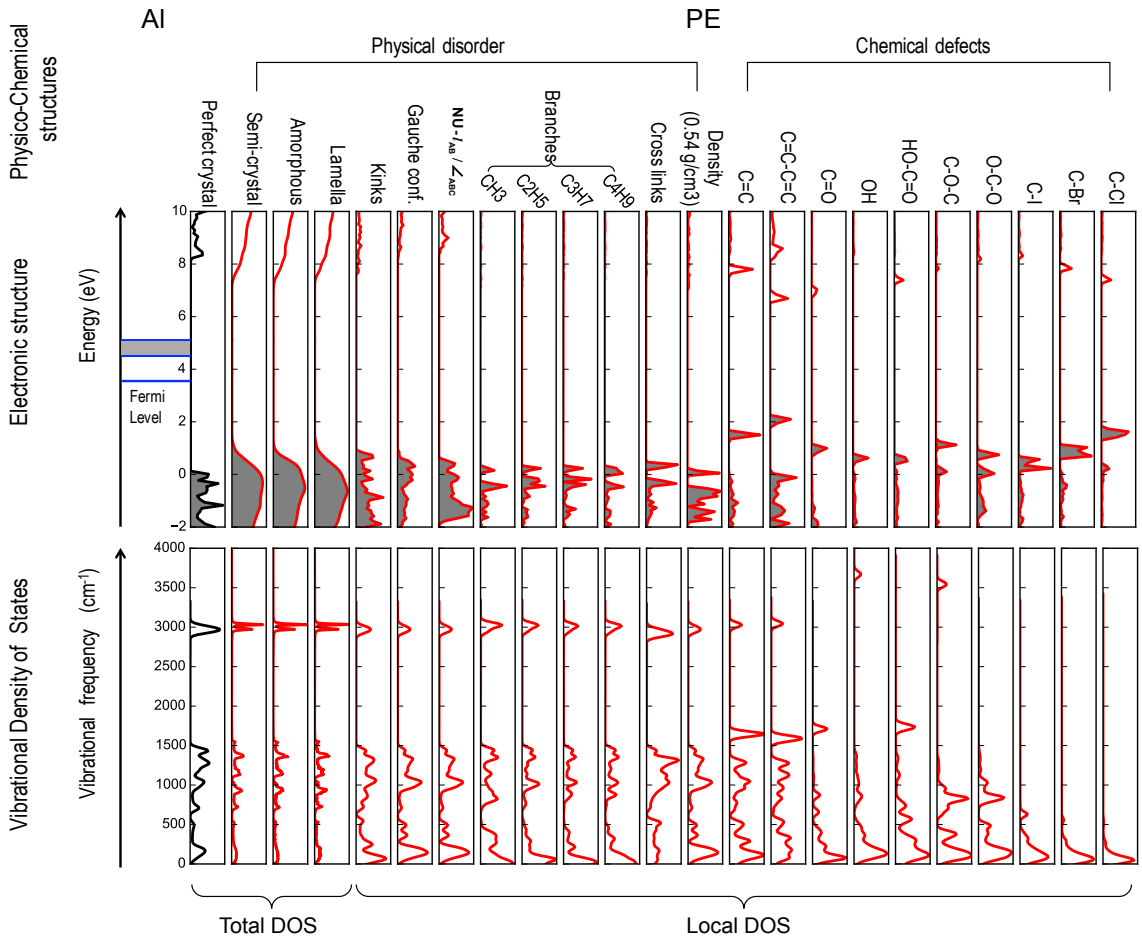

Figure 8.1: Relationships between physico-chemical structures and the relevant properties (i.e., the electronic structure and vibrational behaviors) of PE.

this polymer, including chemical, physical, interfacial, and morphological defects and disorders. By constructing enormous models and properly combining the beyond-conventional DFT with MD simulations, the proposed computational approach has reached an excellent level of accuracy in determining defect levels, activation energies, trap depths of PE, and the charge injection barriers at the interface between PE and Al electrodes.

2. Vibrational density of states of PE:

A complete picture of the vibrational density of states of bulk PE, including physical disorders and chemical defects, has been provided. Using either DFT or classical MD simulations, the computed vibrational frequencies and the resulting heat capacity at constant volume are consistent with experimental values.

3. By combining the electronic structure and vibrational density of states, some "weak points" in PE can be identified, including C=C, C=C–C=C, C=O and O=C–OH. Deep electronic defect states and low vibrational frequencies are introduced by these defects. The former can enhance the electron transport and the latter can slow the heat transport by phonon scattering. This may result in the local overheating around these defects, probably leading to bond breakage due to their low vibrational frequencies (i.e., low bond energies).

8.2 Impacts

Key findings above provide a basis not only to better understand the existing experimental data involving thermal activation energies, luminescence characteristics, IR peaks and heat capacities, but also to fundamentally understand the high field conduction and the heat transport within PE. In addition, computed results can be used as input variables for building phenomenological transport models in which the densities and trap depths of various defects and charge injection barriers are required.

Overall, an understanding of the relationships between physico-chemical structures and these two key properties could take us a step closer to *track, diagnose and impede* polymer degradation and the *rational design* of breakdown-resistant polymer dielectrics.

8.3 Future Work

This thesis discusses the relationships between physico-chemical structures and the electronic structure and vibrational behavior. While these two properties are fundamental to understand the electrical degradation, the following issues are also critical and may be investigated in the future.

1. *Impacts from the external electric field*:

   According to the electronic structure and vibrational behavior, among numerous possible imperfections, chemical defects such as carbonyl (C=O) are the weak points of polymers. The electric field can induce excited states in such pre-existing defects, resulting in the bond cleavage and additional defect formation. Therefore, a knowledge of such chemical processes under the electric field is critical to understand the electrical degradation.

2. *Electronics of electrode/PE interfaces*:

   Charge injection at electrode/PE interfaces is the main source of free carriers within PE. Results in the thesis reveal that charge injection barriers can be decreased from 5 eV into 1 eV, when oxygen-containing groups are introduced

in the interfaces. This may lead to the fact that more free carriers are injected into PE, but these free carriers can be trapped by oxygen-containing groups due to their deep trap depths. As a result, few carriers move into the bulk PE. In fact, this provides a way to prevent space charge accumulations within PE [87]. Therefore, a rational design of electrodes/PE interfaces tailored to desired properties may be the future work. DFT efforts can be used to identify the promising metal electrodes or chemical/physical modifications of interfaces in terms of the charge injection barriers.

3. *Relationship between physico-chemical structures and thermal conductivity*:

   As mentioned in the thesis, thermal conductivity (k) is a key property of polymers, determining the heat transport within PE. It is well known that physico-chemical disorders/defects can enhance the phonon scattering, resulting in a decrease in k. However, the nature of this process has not been fully understood so far. Some computational work has been performed to study the k of polymers with classical MD simulations, but it is limited by the accuracy of anharmonic forces computed by the force fields [88]. DFT is an alternative way to study the k. Recently, Carbogno developed an *Ab-initio* Green-Kubo approach to compute the k of solids, which overcame the lack of high order anharmonicity in the past method [89]. Therefore, this method may be promising to study the k of PE.

Bibliography

[1] Peacook AJ (2000) *Handbook of Polyethylene: Structures: Properties, and Applications.* (Taylor & Francis, NY, USA).

[2] Mayoux C (1997). *IEEE Trans. Dielectr. Electr. Insul.* 4(6):665–673.

[3] Mullin WF (1961) *Understanding capacitors and their uses.* (HW Sams).

[4] Chu B et al. (2006). *Science* 313(5785):334–336.

[5] Huan TD et al. (2016). *Prog. Mater. Sci.* 83:236.

[6] Yoon MH, Yan H, Facchetti A, Marks TJ (2005). *J. Am. Chem. Soc.* 127(29):10388–10395.

[7] Roberts ME et al. (2009). *Chem. Mater.* 21(11):2292–2299.

[8] Dissado LA, Fothergill JC (1992) *Electrical Degradation and Breakdown in Polymers.* (IET, London, UK).

[9] Hawkins WL (1984) *Polymer Degradation and Stabilization.* (Springer-Verlag, Berlin).

[10] Allen NS, Edge M (1993) *Fundamentals of Polymer Degradation and Stabilization.* (Springer, Netherlands).

[11] Martinez-Vega J (2013) *Dielectric materials for electrical engineering.* (John Wiley & Sons).

[12] Teyssedre G, Laurent C (2005). *IEEE Trans. Dielectr. Electr. Insul.* 12:857–875.

[13] Wang C et al. (2014). *Polymer* 55(4):979–988.

[14] Urban MW, Craver CD (1993) *Structure-Property Relations in Polymers* eds. W. UM, D. CC. (American Chemical Society, Washington, DC).

[15] Allen N, Homer J, McKellar J, Wood D (1977). *J. Appl. Polym. Sci.* 21(11):3147–3152.

[16] Qiao B, Teyssedre G, Laurent C (2015). *J. Phys. D: Appl. Phys.* 48(40):405102.

[17] Taleb M, Teyssedre G, Roy S, Laurent C (2013). *IEEE Trans. Dielectr. Electr. Insul.* 20(1):311–320.

[18] Bealing CR, Ramprasad R (2013). *J. Chem. Phys,* 139(17):174904.

[19] Chen L, Tran HD, Wang C, Ramprasad R (2015). *J. Chem. Phys.* 143(12):124907.

[20] Huzayyin A, Boggs S, Ramprasad R (2010). *IEEE Trans. Dielectr. Electr. Insul.* 17(3):926–930.

[21] Wang Y, MacKernan D, Cubero D, Coker DF, Quirke N (2014). *J. Chem. Phys.* 140(15):154902.

[22] Chen L, Huan TD, Quintero YC, Ramprasad R (2016). *J. Mater. Sci.* 51(1):506–512.

[23] Gardette M et al. (2013). *Polym. Degrad. Stab.* 98(11):2383 – 2390.

[24] Corrales T, Catalina F, Peinado C, Allen N, Fontan E (2002). *J. Photochem. Photobiol. A: Chem.* 147(3):213 – 224.

[25] Tarducci C, Kinmond EJ, Badyal JPS, Brewer SA, Willis C (2000). *Chem. Mater.* 12(7):1884–1889.

[26] Laurent C, Mayoux C, Noel S (1985). *J. Appl. Phys.* 58(11):4346–4353.

[27] Laurent C, Teyssedre G, Le Roy S, Baudoin F (2013). *IEEE Trans. Dielectr. Electr. Insul.* 20(2):357–381.

[28] (2013) Infrared spectroscopy.

[29] Meunier M, Quirke N, Aslanides A (2001). *J. Chem. Phys.* 115(6):2876–2881.

[30] Hohenberg P, Kohn W (1964). *Phys. Rev.* 136(3B):B864.

[31] Kohn W, Sham L (1965). *Phys. Rev.* 140:A1133.

[32] Jorgensen WL, Tirado-Rives J (1988). *J. Am. Chem. Soc.* 110(6):1657–1666. PMID: 27557051.

[33] Senftle TP et al. (2016). *npj Computational Materials* 2:15011.

[34] Anta J, Marcelli G, Meunier M, Quirke N (2002). *J. Appl. Phys.* 92(2):1002–1008.

[35] Huzayyin A, Boggs S, Ramprasad R (2010). *IEEE Trans. Dielectr. Electr. Insul.* 17(3):920–925.

[36] Huzayyin A, Boggs S, Ramprasad R (2011) Quantum mechanical study of charge injection at the interface of polyethylene and platinum in *IEEE Conference on Electrical Insulation and Dielectric Phenomena.* (IEEE, IEEE, Cancun), pp. 800–803.

[37] Becke AD (2014). *J. Chem. Phys.* 140(18):18A301.

[38] Zhu H (2012). *ProQuest Dissertations and Theses* p. 143.

[39] Marsman M (2009) Linear response, dielectric properties, *gw* - vasp.

[40] Van de Walle CG, Neugebauer J (2004). *J. Appl. Phys.* 95(8):3851–3879.

[41] Freysoldt C et al. (2014). *Rev. Mod. Phys.* 86:253–305.

[42] Ramprasad R, Zhu H, Rinke P, Scheffler M (2012). *Phys. Rev. Lett.* 108:066404.

[43] Zhu H, Ramprasad R (2011). *Phys. Rev. B* 83(8):081416.

[44] Cardona Quintero Y, Zhu H, Ramprasad R (2013). *J. Mater. Sci.* 48:2277.

[45] Van de Walle CG, Martin RM (1987). *Phys. Rev. B* 35:8154–8165.

[46] Togo A, Tanaka I (2015). *Scr. Mater.* 108:1–5.

[47] Petrenko R, Meller J (2010). *eLS*.

[48] Watkins EK, Jorgensen WL (2001). *J. Phys. Chem. A* 105(16):4118–4125.

[49] Mattsson TR et al. (2010). *Phys. Rev. B* 81:054103.

[50] Stuart SJ, Tutein AB, Harrison JA (2000). *J. Chem. Phys.* 112(14):6472–6486.

[51] Chenoweth K, van Duin ACT, Goddard WA (2008). *J. Phys. Chem. A* 112(5):1040–1053.

[52] Montanari B, Jones R (1997). *Chem. Phys. Lett.* 272(5):347–352.

[53] Sun H (1998). *J. Phys. Chem. B* 102(38):7338–7364.

[54] Androsch R, Di Lorenzo ML, Schick C, Wunderlich B (2010). *Polymer* 51(21):4639–4662.

[55] Kresse G, Furthmüller J (1996). *Phys. Rev. B* 54:11169.

[56] Monkhorst HJ, Pack JD (1976). *Phys. Rev. B* 13:5188.

[57] Perdew JP, Burke K, Ernzerhof M (1996). *Phys. Rev. Lett.* 77(18):3865.

[58] Tkatchenko A, Scheffler M (2009). *Phys. Rev. Lett.* 102(7):073005.

[59] Plimpton S (1995). *J. Comput. Phys.* 117(1):1–19.

[60] Serra S, Tosatti E, Iarlori S, Scandolo S, Santoro G (2000). *Phys. Rev. B* 62:4389–4393.

[61] Ieda M (1984). *IEEE Trans. Electr. Insul.* pp. 162–178.

[62] Lewis T, Llewellyn J (2013). *J. Appl. Phys.* 113(22):223705.

[63] Mizutani T (2006) Behavior of charge carriers in organic insulating materials in *Conference on Electrical Insulation and Dielectric Phenomena*. (IEEE, MO, USA), pp. 1–10.

[64] Mizutani T, Ieda M (1979). *J. Phys. D: Appl. Phys.* 12(2):291.

[65] Yoshino K, Kyokane J, Nishitani T, Inuishi Y (1978). *J. Appl. Phys.* 49(9):4849–4853.

[66] Cheng SZ (2008) *Phase transitions in polymers: the role of metastable states*. (Elsevier).

[67] Friedrich J (2012) *The plasma chemistry of polymer surfaces: advanced techniques for surface design*. (John Wiley & Sons).

[68] Davies DK (1972). *J. Phys. D: Appl. Phys.* 5(1):162.

[69] Chen L, Huan TD, Ramprasad R (2017). *Sci. Rep.* 7(1):6128.

[70] Mizutanim T (2005) Behavior of charge carriers near metal/polymer interface in *Proceedings of the 2005 International Symposium on Electrical Insulating Materials*. (IEEE, IEEE, Japan), Vol. 1, pp. 1–6.

[71] Tanaka T (2001) Space charge injected via interfaces and tree initiation in polymers in *IEEE Conference on Electrical Insulation and Dielectric Phenomena*. (IEEE, IEEE, Kitchener,Ont), pp. 1–15.

[72] Taleb M, Teyssèdre G, Le Roy S (2009) Role of the interface on charge build-up in a low-density polyethylene: Surface roughness and nature of the electrode in *IEEE Conference on Electrical Insulation and Dielectric Phenomena*. (IEEE, IEEE, Virginia Beach, VA), pp. 112–115.

[73] Van de Walle CG, Martin RM (1987). *Phys. Rev. B* 35:8154–8165.

[74] Ramprasad R, Shi N, Tang C (2010) Modeling the physics and chemistry of interfaces in nanodielectrics in *Dielectric Polymer Nanocomposites*. (Springer, New York), pp. 133–161.

[75] Avitabile G et al. (1975). *J. Polym. Sci. Polym. Lett. Ed.* 13:351.

[76] Kittel C (2004) *Introduction to Solid State Physics*. (Wiley, New York), 8 edition.

[77] Haynes WM (2012) *CRC handbook of chemistry and physics*. (CRC press, Boca Raton, FL).

[78] Todorova M, Reuter K, Scheffler M (2004). *J. Phys. Chem. B* 108(38):14477–14483.

[79] Less K, Wilson E (1973). *J. Phys. C* 6(21):3110.

[80] Ishii H, Sugiyama K, Ito E, Seki K (1999). *Adv. Mater.* 11(8):605–625.

[81] Ito E et al. (1998). *Chem. Phys. Lett.* 287:137.

[82] Taylor DM, Lewis TJ (1971). *J. Phys. D: Appl. Phys.* 4:1346.

[83] Mittal KL (2004) *Polymer surface modification: relevance to adhesion.* (CRC Press) Vol. 3.

[84] Ishii H et al. (1998). *IEEE J. Sel. Top. Quant. Electron* 4(1):24–33.

[85] Barrera GD, Parker SF, Ramirez-Cuesta AJ, Mitchell PCH (2006). *Macromolecules* 39(7):2683–2690.

[86] Wilhelm E, Letcher T (2010) *Heat capacities: liquids, solutions and vapours.* (Royal Society of Chemistry).

[87] Teyssedre G et al. (2017). *IEEE Trans. Dielectr. Electr. Insul.* 24(3):1319–1330.

[88] Zhang T, Wu X, Luo T (2014). *J. Phys. Chem. C* 118(36):21148–21159.

[89] Carbogno C, Ramprasad R, Scheffler M (2017). *Phys. Rev. Lett.* 118:175901.

Appendix A

OPLS and Reactive Force Fields

In this appendix, potential energies (U) included in reactive and OPLS force fields are introduced in detail.

A.1 OPLS Force Field

In OPLS force field [48, 49], the total potential energy is expressed as

$$U = U_{\text{bond}} + U_{\text{ang}} + U_{\text{tor}} + U_{\text{nonbond}}. \tag{A.1}$$

Here, bonded (U_{bond}) and angular (U_{ang}) interactions are computed with harmonic potential functions, defined as Eq. (A.2) and Eq. (A.3), respectively,

$$U_{\text{bond}} = \frac{1}{2} k_r (r - r_0)^2, \tag{A.2}$$

$$U_{\text{ang}} = \frac{1}{2} k_\theta (\theta - \theta_0)^2. \tag{A.3}$$

k_r and k_θ are bonded and angular force constants, respectively. r_0 and θ_0 are the equilibrium bond distance and angel, respectively. The torsional potential (U_{tor}) for OPLS is written by [48]

$$U_{\text{tor}} = \sum_{i=1}^{4} \frac{1}{2} K_i [1 - \cos(i\phi)], \tag{A.4}$$

where K_i is the fourier coefficient and ϕ is the torsional angel. U_{nonbond} includes Coulomb's and Lennard-Jones terms, defined by

$$U_{\text{nonbond}} = 4\epsilon_{ij}[(\frac{\sigma_{ij}}{r_{ij}})^{12} - \frac{\sigma_{ij}}{r_{ij}})^6] + k_{coul}\frac{q_i q_j}{r_{ij}}. \tag{A.5}$$

Here ϵ_{ij} and σ_{ij} are well-depths and Lennard-Jones radii for the ij pair, respectively. q_i is the partial charge of atom i and k_{coul} is the coulomb force constant.

Detailed parameters used in OPLS based MD simulations are as follows.

```
pair_coeff    2    2 lj/cut/coul/long     0.030000     2.500000  # H H
pair_coeff    1    1 lj/cut/coul/long     0.065999     3.500000  # C2H
C2H
bond_coeff   2  harmonic  268.0  1.529    # CT-CT
bond_coeff   1  harmonic  340.0  1.090    # CT-HC
angle_coeff  3  harmonic  58.35 112.7    # CT-CT-CT
angle_coeff  1  harmonic  37.5  110.7    # CT-CT-HC
angle_coeff  2  harmonic  33.0  107.8    # HC-CT-HC
dihedral_coeff 1 opls 0.000 0.000 0.3 0.000 # CT-CT-CT-HC
dihedral_coeff 2 opls 0.000 0.000 0.3 0.000 # HC-CT-CT-HC
dihedral_coeff 3 opls 1.300000    -0.050000     0.200000     0.000000
# CT-CT-CT-CT
```

A.2 Reactive Force Field

Reactive Force Field (ReaxFF) is an empirical force field, but its parameters are derived from quantum mechanics calculations [33]. In this force field, the total potential energy (U_{system}) includes the bond energies (U_{bond}), the under-coordination penalty energies (U_{under}), lone-pair energies (U_{lp}), over-coordination penalty energies (U_{over}), valence angle energies (U_{val}), energy penalty forhandling atoms with

two double bonds (U_{pen}), torsion angle energies (U_{tors}), conjugated bond energies (U_{conj}), and terms to handle non-bonded interactions, e.g., van der Waals interactions (U_{vdW}), and coulomb interactions (U_{Coulomb}), expressed as

$$U_{\text{system}} = U_{\text{bond}}+U_{\text{under}}+U_{\text{lp}}+U_{\text{over}}+U_{\text{val}}+U_{\text{val}}+U_{\text{tors}}+U_{\text{conj}}+U_{\text{vdW}}+U_{\text{Coulomb}}. \quad \text{(A.6)}$$

In this force field, in order to realize smooth transitions of bond formation and bond dissociation, the bond energy is determined by bond-orders (BO_{ij}) of the ij pair, expressed as

$$BO_{ij} = BO_{ij}^{\sigma}+BO_{ij}^{\pi}+BO_{ij}^{\pi\pi} = exp[A_{bo1}(\frac{r_{ij}}{r_o^{\sigma}})^{A_{bo2}}]+exp[A_{bo3}(\frac{r_{ij}}{r_o^{\pi}})^{A_{bo4}}]+exp[A_{bo5}(\frac{r_{ij}}{r_o^{\pi\pi}})^{A_{bo6}}]. \quad \text{(A.7)}$$

r_{ij} is the distance between particle i and j; r_o^{σ}, r_o^{π} and $r_o^{\pi\pi}$ correspond to the relaxed bond length of single, double, and triple bonds. A are related parameters [33]. In favor of bond orders, the pair-wise bonded interaction potential is given as

$$U_{\text{bond}} = -D_e^{\sigma}BO_{ij}^{\sigma}exp[p_{be1}(1-(BO_{ij}^{\sigma})^{p_{be2}})] - D_e^{\pi}BO_{ij}^{\pi} - D_e^{\pi\pi}BO_{ij}^{\pi\pi}. \quad \text{(A.8)}$$

where D_e^{σ} and BO_{ij}^{σ} are the dissociation energy and the bond order for the σ bond. Likewise, D_e^{π} and BO_{ij}^{π}, and $D_e^{\pi\pi}$ and $BO_{ij}^{\pi\pi}$ correspond to that of double and triple bonds, respectively. Potentials related to torsion (U_{torsion}) are defined with similar bond-order dependent functions. ReaxFF used in this work was trained from PETN [51], of which parameters are as follows.

```
Reactive MD-force field: PETN
 39       ! Number of general parameters
   50.0000 !Overcoordination parameter
    9.4514 !Overcoordination parameter
   10.8465 !Valency angle conjugation parameter
    3.0000 !Triple bond stabilisation parameter
    6.5000 !Triple bond stabilisation parameter
    0.0000 !C2-correction
    1.0701 !Undercoordination parameter
    9.0000 !Triple bond stabilisation parameter
   11.9083 !Undercoordination parameter
   13.3822 !Undercoordination parameter
    0.0000 !Triple bond stabilization energy
    0.0000 !Lower Taper-radius
   10.0000 !Upper Taper-radius
    2.8793 !Not used
   33.8667 !Valency undercoordination
    5.8971 !Valency angle/lone pair parameter
    1.0563 !Valency angle
    2.0384 !Valency angle parameter
    6.1431 !Not used
    6.9290 !Double bond/angle parameter
    0.3989 !Double bond/angle parameter: overcoord
    3.9954 !Double bond/angle parameter: overcoord
   -2.4837 !Not used
    5.8374 !Torsion/BO parameter
   10.0000 !Torsion overcoordination
    1.8820 !Torsion overcoordination
   -1.2327 !Conjugation 0 (not used)
    2.1861 !Conjugation
    1.5591 !vdWaals shielding
    0.0100 !Cutoff for bond order (*100)
    5.0891 !Valency angle conjugation parameter
    3.4807 !Overcoordination parameter
    9.1739 !Overcoordination parameter
    2.1533 !Valency/lone pair parameter
    0.5000 !Not used
   20.0000 !Not used
    5.0000 !Molecular energy (not used)
    0.0000 !Molecular energy (not used)
    0.2807 !Valency angle conjugation parameter
  8    ! Nr of atoms; cov.r; valency;a.m;Rvdw;Evdw;gammaEEM;cov.r2;#
           alfa;gammavdW;valency;Eunder;Eover;chiEEM;etaEEM;n.u.
           cov r3;Elp;Heat inc.;n.u.;n.u.;n.u.;n.u.
           ov/un;val1;n.u.;val3,vval4
 C    1.3646   4.0000  12.0000   1.9823   0.1749   0.8712   1.2394   4.0000
      9.4606   2.1346   4.0000  31.0823  79.5548   5.7254   6.9235   0.0000
      1.2611   0.0000 200.7713   5.7419  33.3951  11.9957   0.8563   0.0000
     -2.8983   2.5000   1.0564   4.0000   2.9663   0.0000   0.0000   0.0000
 H    0.6867   1.0000   1.0080   1.3525   0.0616   0.8910  -0.1000   1.0000
      9.3858   5.0013   1.0000   0.0000 121.1250   3.8446  10.0839   1.0000
     -0.1000   0.0000  63.2739   3.8461   3.2540   1.0000   1.0698   0.0000
    -15.7683   2.1504   1.0338   1.0000   2.8793   0.0000   0.0000   0.0000
 O    1.3142   2.0000  15.9990   1.9741   0.0880   0.8712   1.1139   6.0000
     10.2186   7.7719   4.0000  29.5271 116.0768   8.5000   7.1412   2.0000
      0.9909   6.5561  58.4859   9.2294   1.6620   0.1882   0.9745   0.0000
     -3.5965   2.5000   1.0493   4.0000   2.9225   0.0000   0.0000   0.0000
 N    1.2388   3.0000  14.0000   1.9324   0.1376   0.8922   1.1650   5.0000
     10.0667   7.8431   4.0000  32.4758 100.0000   6.7424   6.2435   2.0000
      1.0589   7.3542 131.6593   1.7889   3.0032   2.7652   0.9745   0.0000
```

```
    -4.0959   2.0047   1.0183   4.0000   2.8793   0.0000   0.0000   0.0000
 S   1.9647   2.0000  32.0600   2.0783   0.2176   1.0336   1.5386   6.0000
     9.9676   5.0812   4.0000  35.1648 112.1416   6.5000   8.2545   2.0000
     1.4703   9.4922  70.0338   8.5146  28.0801   8.5010   0.9745   0.0000
   -10.0773   2.7466   1.0338   6.2998   2.8793   0.0000   0.0000   0.0000
 Si   2.0276   4.0000  28.0600   2.2042   0.1322   0.8218   1.5758   4.0000
    11.9413   2.0618   4.0000  11.8211 136.4845   1.8038   7.3852   0.0000
    -1.0000   0.0000 126.5331   6.4918   8.5961   0.2368   0.8563   0.0000
    -3.8112   3.1873   1.0338   4.0000   2.5791   0.0000   0.0000   0.0000
 Al   2.1892   3.0000  26.9820   1.8538   0.1913   0.8009  -1.6836   3.0000
    12.9825   3.7103   3.0000   0.0076  16.5151   2.1431   6.4606   0.0000
    -1.0000   0.0000  67.5458  49.8470   0.0972   0.0000   0.8563   0.0000
    -6.0000   2.9933   1.0338   3.0000   2.5791   0.0000   0.0000   0.0000
 X   -0.1000   2.0000   1.0080   2.0000   0.0000   1.0000  -0.1000   6.0000
    10.0000   2.5000   4.0000   0.0000   0.0000   8.5000   1.5000   0.0000
    -0.1000   0.0000  -2.3700   8.7410  13.3640   0.6690   0.9745   0.0000
   -11.0000   2.7466   1.0338   6.2998   2.8793   0.0000   0.0000   0.0000
 23      ! Nr of bonds; Edis1;LPpen;n.u.;pbe1;pbo5;13corr;pbo6
                        pbe2;pbo3;pbo4;n.u.;pbo1;pbo2;ovcorr
  1  1 142.2067 113.7374  66.5758   0.1668  -1.1231   1.0000  44.0187
0.4319
       0.0830  -0.2086   8.6394   1.0000  -0.0940   6.6753   1.0000
0.0000
  1  2 163.7782   0.0000   0.0000  -0.4525   0.0000   1.0000   6.0000
0.5956
      12.1068   1.0000   0.0000   1.0000  -0.0097   8.6352   0.0000
0.0000
  2  2 169.8421   0.0000   0.0000  -0.3591   0.0000   1.0000   6.0000
0.7503
       9.3119   1.0000   0.0000   1.0000  -0.0169   5.9406   0.0000
0.0000
  1  3 167.2167 114.1224  81.3938  -0.5005  -0.2883   1.0000  18.6939
0.4977
       1.2418  -0.2763   7.0279   1.0000  -0.1626   4.6449   0.0000
0.0000
  3  3  98.8742 158.1100  40.0000   0.1389  -0.1442   1.0000  25.0595
0.4995
       0.8169  -0.2716   7.8369   1.0000  -0.1064   6.5523   1.0000
0.0000
  1  4 130.0685 158.5881  70.9892   0.0060  -0.1875   1.0000  35.0000
0.3618
       0.0115  -0.3456   7.0651   1.0000  -0.1415   5.1668   1.0000
0.0000
  3  4 107.8111 182.8827  40.0000   0.5261  -0.1944   1.0000  35.0000
0.2000
       0.8345  -0.3263   7.0000   1.0000  -0.1106   6.0520   1.0000
0.0000
  4  4 156.5641  77.2208 167.3656   0.1363  -0.1440   1.0000  12.0000
0.5393
       0.0570  -0.1873  10.5092   1.0000  -0.0844   4.9761   1.0000
0.0000
  2  3 215.7763   0.0000   0.0000  -0.5428   0.0000   1.0000   6.0000
1.6190
       4.7086   1.0000   0.0000   1.0000  -0.0665   5.1983   0.0000
0.0000
  2  4 223.8889   0.0000   0.0000  -0.3923   0.0000   1.0000   6.0000
0.4579
      10.4022   1.0000   0.0000   1.0000  -0.0661   6.0356   0.0000
0.0000
  1  5 128.7959  56.4134  39.0716   0.0688  -0.4463   1.0000  31.1766
```

```
0.4530
        0.1955  -0.3587   6.2148   1.0000  -0.0770   6.6386   1.0000
0.0000
  2  5 128.6090   0.0000   0.0000  -0.5555   0.0000   1.0000   6.0000
0.4721
       10.8735   1.0000   0.0000   1.0000  -0.0242   9.1937   1.0000
0.0000
  3  5   0.0000   0.0000   0.0000   0.5563  -0.4038   1.0000  49.5611
0.6000
        0.4259  -0.4577  12.7569   1.0000  -0.1100   7.1145   1.0000
0.0000
  4  5   0.0000   0.0000   0.0000   0.4438  -0.2034   1.0000  40.3399
0.6000
        0.3296  -0.3153   9.1227   1.0000  -0.1805   5.6864   1.0000
0.0000
  5  5  96.1871  93.7006  68.6860   0.0955  -0.4781   1.0000  17.8574
0.6000
        0.2723  -0.2373   9.7875   1.0000  -0.0950   6.4757   1.0000
0.0000
  6  6 109.1904  70.8314  30.0000   0.2765  -0.3000   1.0000  16.0000
0.1583
        0.2804  -0.1994   8.1117   1.0000  -0.0675   8.2993   0.0000
0.0000
  2  6 137.1002   0.0000   0.0000  -0.1902   0.0000   1.0000   6.0000
0.4256
       17.7186   1.0000   0.0000   1.0000  -0.0377   6.4281   0.0000
0.0000
  3  6 191.1743  52.0733  43.3991  -0.2584  -0.3000   1.0000  36.0000
0.8764
        1.0248  -0.3658   4.2151   1.0000  -0.5004   4.2605   1.0000
0.0000
  3  7 125.7186   0.0000   0.0000  -0.0108  -0.3000   1.0000  36.0000
0.0217
        0.0382  -0.3500  25.0000   1.0000  -0.0841   8.7575   1.0000
0.0000
  1  7 115.8808   0.0000   0.0000  -0.9287  -0.3000   1.0000  36.0000
0.4153
        0.5621  -0.3500  25.0000   1.0000  -0.0590   4.9250   1.0000
0.0000
  4  7  90.4024   0.0000   0.0000   0.6578  -0.3000   1.0000  36.0000
0.2757
        0.3123  -0.3500  25.0000   1.0000  -0.0412   5.4111   1.0000
0.0000
  2  7 127.3523   0.0000   0.0000  -0.0392  -0.3000   1.0000  36.0000
0.0533
        0.2472  -0.3500  25.0000   1.0000  -0.0925   5.0000   1.0000
0.0000
  7  7  48.8623   0.0000   0.0000  -0.4178  -0.3000   0.0000  16.0000
0.3972
        0.1283  -0.4197  14.3085   1.0000  -0.1294   6.3838   0.0000
0.0000
 14    ! Nr of off-diagonal terms; Ediss;Ro;gamma;rsigma;rpi;rpi2
  1  2   0.0410   1.7521  10.3075   1.0334  -1.0000  -1.0000
  2  3   0.0393   1.7873  10.5574   0.8775  -1.0000  -1.0000
  2  4   0.0495   1.7155  10.5841   1.0011  -1.0000  -1.0000
  1  3   0.1146   1.9102   9.6844   1.3551   1.1219   1.1321
  1  4   0.1460   1.7657   9.9620   1.3434   1.1803   1.1130
  3  4   0.0994   1.8754  10.2664   1.2725   1.1046   0.9429
  2  6   0.0470   1.6738  11.6877   1.1931  -1.0000  -1.0000
  3  6   0.1263   1.8163  10.6833   1.6266   1.2052  -1.0000
```

```
 3  7   0.1000   1.7303  10.5371   1.6278  -1.0000  -1.0000
 1  7   0.1900   1.9000  10.1473   1.6600  -1.0000  -1.0000
 4  7   0.1074   1.7000  10.1626   1.3335  -1.0000  -1.0000
 2  7   0.0515   1.8072  11.0758   1.5063  -1.0000  -1.0000
 1  5   0.1408   1.8161   9.9393   1.7986   1.3021   1.4031
 2  5   0.0895   1.6239  10.0104   1.4640  -1.0000  -1.0000
99    ! Nr of angles;at1;at2;at3;Thetao,o;ka;kb;pv1;pv2
 1  1  1  73.9461  32.5133   0.9462   0.0000   0.1780  10.5736   1.0400
 1  1  2  70.6814  14.3470   5.3791   0.0000   0.0058   0.0000   1.0400
 2  1  2  76.7511  14.4234   3.3613   0.0000   0.0127   0.0000   1.0400
 1  2  2   0.0000   0.0000   6.0000   0.0000   0.0000   0.0000   1.0400
 1  2  1   0.0000   3.4110   7.7350   0.0000   0.0000   0.0000   1.0400
 2  2  2   0.0000  27.9213   5.8635   0.0000   0.0000   0.0000   1.0400
 1  1  3  58.3933  11.1817   4.0095   0.0000   0.5040  10.0000   1.0683
 3  1  3  79.1659  45.0000   1.3710   0.0000   0.5040   0.0000   1.0683
 1  1  4  58.5570  22.9823   1.7699   0.0000   0.5040  10.0000   1.0683
 3  1  4  71.8297  32.0036   2.8362   0.0000   0.5040   0.0000   1.0683
 4  1  4  88.9289  17.8225   0.6509   0.0000   0.5040   0.0000   1.0683
 2  1  3  52.2377  11.7910   7.4347   0.0000   0.8817   0.0000   1.0400
 2  1  4  66.7848  20.0781   3.2493   0.0000   0.8817   0.0000   1.0400
 1  2  4   0.0000   0.0019   6.3000   0.0000   0.0000   0.0000   1.0400
 1  3  1  89.3429  44.3536   0.6873   0.0000   0.8209   0.0000   1.0422
 1  3  3  80.9125  45.0000   0.2688   0.0000   0.8209   0.0000   1.0422
 1  3  4  76.2335   9.0759   6.1320   0.0000   0.8209   0.0000   1.0422
 3  3  3  87.8004  20.3951   2.0002 -10.0000   0.8209   0.0000   1.0422
 3  3  4  86.3737  23.8196   1.9027   0.0000   0.8209   0.0000   1.0422
 4  3  4  69.4285  44.7630   2.1367   0.0000   0.8209   0.0000   1.0422
 1  3  2  76.9669  41.5636   0.7950   0.0000   0.4420   0.0000   1.0400
 2  3  3  77.0499   5.6157   7.5000   0.0000   0.4420   0.0000   1.0400
 2  3  4  77.1454  45.0000   1.9924   0.0000   0.4420   0.0000   1.0400
 2  3  2  80.0246  12.7196   4.7459   0.0000   0.2768   0.0000   1.0400
 1  4  1  65.3740   8.1740   0.8938   0.0000   1.3684   0.0000   1.0686
 1  4  3  89.5500  27.4315   1.4132   0.0000   1.3684   0.0000   1.0686
 1  4  4  76.9932  28.8033   1.7703   0.0000   1.3684   0.0000   1.0686
 3  4  3  75.3010  32.6234   1.1339 -13.2118   1.3684   0.0000   1.0686
 3  4  4  88.3613  45.0000   0.6312  -0.9193   1.3684   0.0000   1.0686
 4  4  4  71.8573  34.0804   3.0431   0.0000   1.3684   0.0000   1.0686
 1  4  2  90.0000  32.4158   1.0529   0.0000   0.2065   0.0000   1.0445
 2  4  3  83.5629  42.8281   1.6511   0.0000   0.2065   0.0000   1.0445
 2  4  4  76.0974  15.5545   3.6730   0.0000   0.2065   0.0000   1.0445
 2  4  2  53.1308   9.9577   5.2535   0.0000   0.2807   0.0000   3.0000
 1  2  3   0.0000   0.0019   6.0000   0.0000   0.0000   0.0000   1.0400
 1  2  4   0.0000   0.0019   6.0000   0.0000   0.0000   0.0000   1.0400
 1  2  5   0.0000   0.0019   6.0000   0.0000   0.0000   0.0000   1.0400
 3  2  3   0.0000   0.0019   6.0000   0.0000   0.0000   0.0000   1.0400
 3  2  4   0.0000   0.0019   6.0000   0.0000   0.0000   0.0000   1.0400
 4  2  4   0.0000   0.0019   6.0000   0.0000   0.0000   0.0000   1.0400
 2  2  3   0.0000   0.0019   6.0000   0.0000   0.0000   0.0000   1.0400
 2  2  4   0.0000   0.0019   6.0000   0.0000   0.0000   0.0000   1.0400
 1  1  5  74.9397  25.0560   1.8787   0.1463   0.0559   0.0000   1.0400
 1  5  1  86.9521  36.9951   2.0903   0.1463   0.0559   0.0000   1.0400
 2  1  5  74.9397  25.0560   1.8787   0.0000   0.0000   0.0000   1.0400
 1  5  2  86.1791  36.9951   2.0903   0.0000   0.0000   0.0000   1.0400
 1  5  5  85.3644  36.9951   2.0903   0.1463   0.0559   0.0000   1.0400
 2  5  2  93.1959  36.9951   2.0903   0.0000   0.0000   0.0000   1.0400
 2  5  5  84.3331  36.9951   2.0903   0.0000   0.0000   0.0000   1.0400
 6  6  6  69.3456  21.7361   1.4283   0.0000  -0.2101   0.0000   1.3241
 2  6  6  75.6168  21.5317   1.0435   0.0000   2.5179   0.0000   1.0400
 2  6  2  78.3939  20.9772   0.8630   0.0000   2.8421   0.0000   1.0400
 3  6  6  70.3016  15.4081   1.3267   0.0000   2.1459   0.0000   1.0400
```

```
 2  6  3  73.8232  16.6592   3.7425   0.0000   0.8613   0.0000   1.0400
 3  6  3  90.0344   7.7656   1.7264   0.0000   0.7689   0.0000   1.0400
 6  3  6  22.1715   3.6615   0.3160   0.0000   4.1125   0.0000   1.0400
 2  3  6  83.7634   5.6693   2.7780   0.0000   1.6982   0.0000   1.0400
 3  3  6  73.4663  25.0761   0.9143   0.0000   2.2466   0.0000   1.0400
 2  2  6   0.0000  47.1300   6.0000   0.0000   1.6371   0.0000   1.0400
 6  2  6   0.0000  31.5209   6.0000   0.0000   1.6371   0.0000   1.0400
 3  2  6   0.0000  31.0427   4.5625   0.0000   1.6371   0.0000   1.0400
 2  2  5   0.0000   0.0019   6.0000   0.0000   0.0000   0.0000   1.0400
 2  3  7  90.0000   9.6286   3.2827   0.0000   1.0000   0.0000   1.1000
 3  3  7  43.6647  40.0000   5.0000   0.0000   1.0000   0.0000   2.0166
 3  7  3  44.6561  38.0442   2.4731   0.0000   1.0000   0.0000   2.9818
 2  1  7  80.0000  25.0000   2.0000   0.0000   1.0000   0.0000   1.0500
 1  1  7  70.0000  30.0000   2.0000   0.0000   1.0000   0.0000   1.0500
 1  7  1  85.0000  40.0000   1.1464   0.0000   1.0000   0.0000   2.0191
 2  4  7  70.0000  25.0000   2.0000   0.0000   1.0000   0.0000   1.0500
 4  4  7  70.0000  30.0000   2.0000   0.0000   1.0000   0.0000   1.0500
 4  7  4  49.1319  27.6649   3.6319   0.0000   1.0000   0.0000   2.8783
 7  3  7  31.5896  13.7247   5.0000   0.0000   1.0000   0.0000   2.9866
 7  4  7  80.3242  40.0000   5.0000   0.0000   1.0000   0.0000   1.4147
 1  7  2  69.7915  24.1030   0.8107   0.0000   1.0000   0.0000   1.5000
 2  7  2  69.0938  40.0000   0.6513   0.0000   1.0000   0.0000   1.1000
 2  7  3  63.8918  36.1946   1.4757   0.0000   1.0000   0.0000   2.1056
 2  7  4  78.3632  19.2322   1.5955   0.0000   1.0000   0.0000   1.5000
 3  7  4  67.0745  37.6673   1.4614   0.0000   1.0000   0.0000   1.1000
 1  7  3  71.0541  29.4591   0.8520   0.0000   1.0000   0.0000   1.1000
 1  7  4  71.1428  32.9676   0.9187   0.0000   1.0000   0.0000   1.1000
 1  3  7  70.0000  30.0000   2.0000   0.0000   1.0000   0.0000   1.0500
 3  1  7  70.0000  30.0000   2.0000   0.0000   1.0000   0.0000   1.0500
 1  4  7  70.0000  30.0000   2.0000   0.0000   1.0000   0.0000   1.0500
 4  1  7  70.0000  30.0000   2.0000   0.0000   1.0000   0.0000   1.0500
 1  4  7  70.0000  30.0000   2.0000   0.0000   1.0000   0.0000   1.0500
 4  3  7  70.0000  30.0000   2.0000   0.0000   1.0000   0.0000   1.0500
 7  1  7  50.0000  20.0000   1.0000   0.0000   1.0000   0.0000   1.1000
 7  2  1   0.0000  20.0000   1.0000   0.0000   1.0000   0.0000   1.1000
 7  2  2   0.0000  20.0000   1.0000   0.0000   1.0000   0.0000   1.1000
 7  2  3   0.0000  20.0000   1.0000   0.0000   1.0000   0.0000   1.1000
 7  2  4   0.0000  20.0000   1.0000   0.0000   1.0000   0.0000   1.1000
 7  2  7   0.0000  20.0000   1.0000   0.0000   1.0000   0.0000   1.1000
 3  7  7  24.7294   2.1936   1.8857   0.0000   1.0000   0.0000   1.1000
 2  7  7  48.7851  40.0000   5.0000   0.0000   1.0000   0.0000   1.3503
 1  7  7  26.2759   2.3895   1.0406   0.0000   1.0000   0.0000   1.1505
 4  7  7  26.2759   0.2500   1.0000   0.0000   1.0000   0.0000   1.1505
 1  2  7   0.0000   5.0000   1.0000   0.0000   1.0000   0.0000   1.5000
 3  2  7   0.0000   5.0000   1.0000   0.0000   1.0000   0.0000   1.5000
 4  2  7   0.0000   5.0000   1.0000   0.0000   1.0000   0.0000   1.5000
23    ! Nr of torsions;at1;at2;at3;at4;;V1;V2;V3;V2(BO);vconj;n.u;n
 1  1  1  1   0.0000  48.4194   0.3163  -8.6506  -1.7255   0.0000   0.0000
 1  1  1  2   0.0000  63.3484   0.2210  -8.8401  -1.8081   0.0000   0.0000
 2  1  1  2   0.0000  45.2741   0.4171  -6.9800  -1.2359   0.0000   0.0000
 0  1  2  0   0.0000   0.0000   0.0000   0.0000   0.0000   0.0000   0.0000
 0  2  2  0   0.0000   0.0000   0.0000   0.0000   0.0000   0.0000   0.0000
 0  1  3  0  -0.0020  83.7039   0.5032  -4.4955  -2.0000   0.0000   0.0000
 0  2  3  0   0.0000   0.1000   0.0200  -2.5415   0.0000   0.0000   0.0000
 0  3  3  0   0.0002 150.0000   0.0002  -5.1965   0.0000   0.0000   0.0000
 0  1  4  0  -0.3338 150.0000   0.4498  -6.6900  -2.0000   0.0000   0.0000
 0  2  4  0   0.0000   0.1000   0.0200  -2.5415   0.0000   0.0000   0.0000
 0  3  4  0   1.9343 144.4475  -0.3610  -8.2060  -2.0000   0.0000   0.0000
 0  4  4  0  -2.0000 150.0000  -1.5000  -5.3739  -2.0000   0.0000   0.0000
 0  1  1  0   0.0930  22.6165   0.0002  -8.9043  -1.0000   0.0000   0.0000
```

```
4  1  4  4  -2.0000  10.0000  -1.5000  -9.0000  -2.0000   0.0000   0.0000
0  1  5  0   4.0885  78.7058   0.1174  -2.1639   0.0000   0.0000   0.0000
0  5  5  0  -0.0170 -56.0786   0.6132  -2.2092   0.0000   0.0000   0.0000
0  2  5  0   0.0000   0.0000   0.0000   0.0000   0.0000   0.0000   0.0000
0  6  6  0   0.0000   0.0000   0.1200  -2.4426   0.0000   0.0000   0.0000
0  2  6  0   0.0000   0.0000   0.1200  -2.4847   0.0000   0.0000   0.0000
0  3  6  0   0.0000   0.0000   0.1200  -2.4703   0.0000   0.0000   0.0000
1  1  3  3  -0.0002  80.0000   1.5000  -9.0000  -2.0000   0.0000   0.0000
1  3  3  1   0.0002  80.0000  -1.5000  -3.1276  -2.0000   0.0000   0.0000
3  1  3  3  -0.1249  61.1242   1.5000  -9.0000  -2.0000   0.0000   0.0000
9    ! Nr of hydrogen bonds;at1;at2;at3;Rhb;Dehb;vhb1
3  2  3   2.0000  -5.0000   2.9784   2.8122
3  2  4   1.8329  -5.0000   2.9784   2.8122
4  2  3   1.2590  -5.0000   2.9784   2.8122
4  2  4   1.7312  -5.0000   2.9784   2.8122
3  2  5   2.6644  -3.9547   2.9784   2.8122
4  2  5   4.0476  -5.7038   2.9784   2.8122
5  2  3   2.1126  -4.5790   2.9784   2.8122
5  2  4   2.2066  -5.7038   2.9784   2.8122
5  2  5   1.9461  -4.0000   2.9784   2.8122
```

A.3 Details of Phase Diagram Calculations

The phase diagram of cystalline PE was calcuated by the predication of the melting point, at which temperature solid crystal PE is changed into its liquid state under the specific pressure. In order to predict the melting point (T_{m}), NPT-MD simulations were performed on a 2 $\times$ 2 $\times$ 10 supercell over 1 ns, using OPLS and ReaxFF respectively. Here, the pressure ranging from 1 to 1000 atm and the temperature in a range of 300 – 700 K were considered. The resulting thermal density variations at 1 atm are summarized in Table A.1 and shown in Fig. A.1. These are average values derived from the final 100 ps relaxations. Fig. A.1 shows that the density decrease sharply at the specific temperature (as denoted by dashed lines), i.e., the melting point (T_{m}).

The computed melting points at differenet pressures are summarized in Table A.2. These T_{m} values can be used to form the phase transition boundary between solid and liquid phases of crystal PE, as denoted by lines with markers in Fig. A.2.

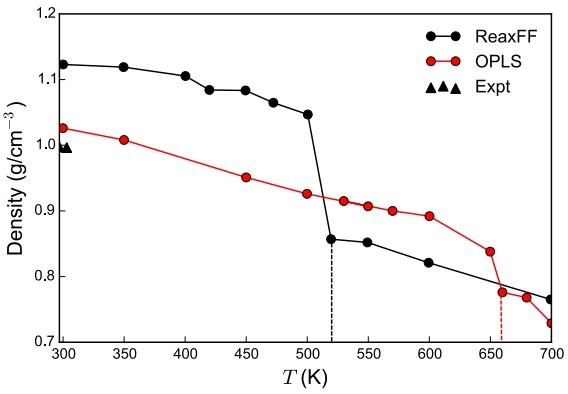

Figure A.1: Thermal density variations (g/cm^3) of crystal PE at pressure of 1 atm, together with experimental data from Ref. [53] (denoted by black triangles).

Table A.1: Thermal density variations at 1 atm, computed by OPLS and ReaxFF.

OPLS		ReaxFF	
T (K)	Density (g/cm3)	T (K)	Density (g/cm3)
300	1.026	300	1.123
350	1.008	350	1.119
450	0.951	400	1.105
500	0.926	420	1.084
530	0.915	449	1.083
550	0.907	472	1.065
570	0.9	500	1.047
600	0.892	519	0.857
650	0.838	549	0.852
660	0.776	599	0.821
680	0.768	699	0.765
700	0.729		

Table A.2: Melting points (T_{m}) at the differenet pressure, along with experimental values from Ref. [54].

Pressure (atm)	T_{m} (K)		
	ReaxFF	OPLS	Expt.
1	520	660	418
250	530	670	420
500	530	680	430
780	532	690	439
1000	539	700	450

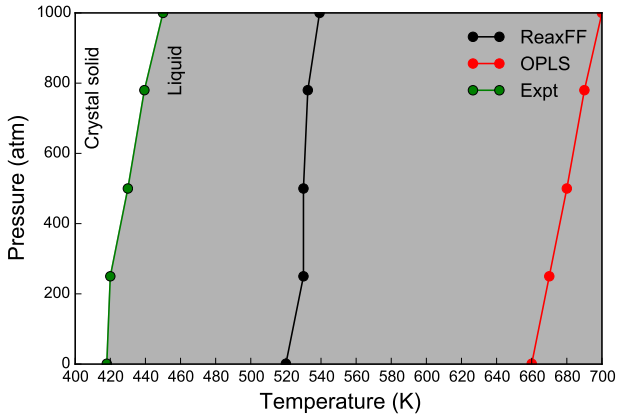

Figure A.2: Computed phase diagram of crystal PE with solid and liquid phases denoted by blank and shaded regions, respectively, along with experimental values from Ref. [54], respectively.

Appendix B

Models and DFT Results of Electronic Structure Calculations

B.1 Details of Models

Table B.1: Detailed information of models used in the electronic structure calculations, including the total number of atom types ($N_{\text{atom type}}$), atoms (N_{total}) and each type of atoms (i.e., N_{C}, N_{H}, N_{O}, and N_{Al}).

Configurations		$N_{\text{atom type}}$	N_{total}	N_{C}	N_{H}	N_{O}	N_{Al}
Perfect crystal		2	12	4	8		
Physical Disorders	Density of 1.03 g/cm3	2	120	40	80		
	Density of 0.98 g/cm^3	2	120	40	80		
	Density of 0.90 g/cm^3	2	120	40	80		
	Density of 0.83 g/cm^3	2	120	40	80		
	Density of 0.77 g/cm^3	2	120	40	80		
	Density of 0.72 g/cm^3	2	120	40	80		
	Density of 0.54 g/cm^3	2	120	40	80		
	Density of 0.36 g/cm^3	2	120	40	80		
	Branches-CH_3	2	123	41	82		
	Branches-C_2H_5	2	126	42	84		
	Branches-C_3H_7	2	129	43	86		
	Branches-C_4H_9	2	132	44	88		
	Cross links (C_5H_8)	2	133	45	88		
	Non-uniform bonds/angles	2	120	40	80		
	Gauch conformations	2	120	40	80		
	Kinks	2	120	40	80		
	Lamella	2	1202	400	802		

	Amorphous region	2	1202	400	802		
	Semi-crystal	2	2402	800	1602		
Chemical Defects	C=C	2	70	24	46		
	C=C-C=C	2	68	24	44		
	$C=CH_2$	2	73	24	48		
	C=O	3	71	24	46	1	
	OH	3	73	24	48	1	
	O=C-OH	3	75	25	48	2	
	C-O-C	3	71	24	46	1	
	O-C-O	3	68	22	44	2	
	C-I	3	72	24	47	1	
	C-Br	3	72	24	47	1	
	C-Cl	3	72	24	47	1	
Al/PE Interfaces	Clean Al/PE	3	312	80	160		72
	Al/PE+C-O-C	4	304	80	144	8	72
	Al/PE+O-C-O	4	296	72	144	8	72
	Al/PE+O=C-OH	4	324	84	160	8	72
	Al/PE+C=O	4	304	80	144	8	72
	Al/PE+OH	4	320	80	160	8	72

B.2 DFT Results

Table B.2 and B.3 list HSE06 CBM, VBM and E_{g} of PE with physical disorders and chemical defects, respectively. PBE E_{C1s} values are also provided, which are the same with HSE06 results. Table B.4 shows 50 data points used to train the relationship between $E_{\mathrm{g}}^{\mathrm{PBE}}$ and $E_{\mathrm{g}}^{\mathrm{HSE06}}$ (i.e. Eq. (2.1)). Table B.5 provides thermodynamic and optical charge transition levels ($E_{(0/\pm1)}^{\mathrm{therm}}$ and $E_{(0\leftrightarrows\pm1)}^{\mathrm{opt}}$) of chemical defects, computed by the HSE06 functional. Table B.6 presents computed vacuum energy shift ($\Delta\varphi$, eV) of Al/PE interfaces with three positions of oxygen-containing groups in the second layer of the interface.

Table B.2: Computed PBE E_{C1s}, and HSE06 CBM, VBM and E_{g} of PE with physical disorders, given in eV. Except for branches and cross links, 10 configurations have been used to compute the electronic structure of the remaining systems. The density ρ of PE (with disorders) is given in g/cm^3.

Configurations	Densities	E_{C1s}	CBM	VBM	E_{g}
Perfect Crystal	1.08	-264.17	5.17	-3.11	8.28
Density Variation	1.03	-264.63	4.92	-3.12	8.04
		-264.64	4.93	-3.13	8.06
		-264.64	4.95	-3.13	8.08
		-264.64	4.96	-3.13	8.09
		-264.64	4.99	-3.13	8.12
		-264.64	5.00	-3.13	8.13
		-264.64	4.99	-3.13	8.12
		-264.64	5.01	-3.13	8.14
		-264.64	5.02	-3.13	8.14
		-264.64	5.02	-3.13	8.15
	0.98	-265.00	4.73	-3.12	7.85
		-265.00	4.76	-3.12	7.88
		-265.00	4.81	-3.12	7.94
		-265.00	4.84	-3.13	7.97
		-264.64	4.87	-3.13	7.99
		-265.01	4.86	-3.13	7.99
		-265.01	4.80	-3.12	7.92
		-265.01	4.88	-3.13	8.01
		-265.01	4.89	-3.13	8.02
		-265.00	4.90	-3.13	8.03
	0.90	-265.30	4.48	-3.12	7.60
		-265.30	4.51	-3.12	7.63
		-265.31	4.56	-3.12	7.68
		-265.31	4.58	-3.12	7.70
		-265.31	4.86	-3.13	7.99
		-265.31	4.65	-3.13	7.78
		-265.31	4.67	-3.13	7.80
		-265.31	4.68	-3.13	7.80
		-265.31	4.68	-3.13	7.81
		-265.31	4.69	-3.13	7.82
	0.83	-265.56	4.33	-3.12	7.45
		-265.56	4.38	-3.12	7.50
		-265.56	4.40	-3.12	7.52
		-265.57	4.46	-3.13	7.58
		-265.57	4.47	-3.13	7.60
		-265.57	4.49	-3.13	7.62
		-265.57	4.51	-3.13	7.64
		-265.58	4.52	-3.13	7.65
		-265.57	4.53	-3.13	7.66
		-265.57	4.53	-3.13	7.66
	0.77	-265.79	4.23	-3.12	7.35
		-265.79	4.24	-3.12	7.36
		-265.79	4.26	-3.12	7.38
		-265.79	4.27	-3.12	7.40
		-265.79	4.33	-3.12	7.46

			-265.80	4.37	-3.13	7.49
			-265.80	4.39	-3.13	7.52
			-265.80	4.40	-3.13	7.53
			-265.80	4.41	-3.13	7.54
			-265.80	4.42	-3.13	7.54
		0.72	-266.58	4.16	-3.12	7.28
			-266.57	4.16	-3.12	7.28
			-266.57	4.18	-3.12	7.30
			-266.57	4.19	-3.12	7.32
			-266.58	4.23	-3.12	7.35
			-266.58	4.24	-3.12	7.37
			-266.58	4.29	-3.13	7.41
			-266.58	4.30	-3.13	7.42
			-266.59	4.28	-3.13	7.41
			-266.58	4.23	-3.13	7.36
		0.54	-267.36	3.89	-3.12	7.01
			-267.35	3.89	-3.13	7.02
			-267.35	3.89	-3.13	7.02
			-267.35	3.89	-3.13	7.02
			-267.35	3.89	-3.12	7.02
			-267.36	3.89	-3.13	7.01
			-267.36	3.90	-3.12	7.02
			-267.36	3.86	-3.13	6.98
			-267.36	3.89	-3.13	7.02
			-267.36	3.84	-3.13	6.97
		0.36	-267.75	3.77	-3.12	6.89
			-267.74	3.74	-3.13	6.86
			-267.74	3.78	-3.13	6.90
			-267.75	3.77	-3.13	6.89
			-267.74	3.75	-3.13	6.88
			-267.74	3.78	-3.13	6.90
			-267.75	3.80	-3.12	6.92
			-267.75	3.89	-3.13	7.02
			-267.75	3.98	-3.13	7.10
			-267.74	4.02	-3.13	7.15
Branches	CH3	0.56	-266.54	3.93	-3.02	6.95
	C2H5	0.57	-266.48	3.95	-2.99	6.94
	C3H7	0.58	-266.42	3.94	-2.99	6.93
	C4H9	0.60	-266.35	3.92	-3.01	6.93
Cross links	C5H8	0.61	-266.45	4.06	-2.84	6.90
Non-uniform bonds/angles		1.08	-264.21	5.12	-2.85	7.98
			-264.20	5.11	-2.95	8.06
			-264.20	5.13	-2.92	8.05
			-264.25	5.13	-2.76	7.89
			-264.24	5.05	-2.81	7.86
			-264.27	5.18	-2.64	7.82
			-264.22	5.08	-2.83	7.91
			-264.21	5.08	-2.78	7.85
			-264.23	5.10	-2.80	7.89
			-264.18	5.03	-2.92	7.95
Gauch conformations		1.08	-264.39	5.21	-2.22	7.43
			-264.36	4.94	-2.00	6.94
			-264.38	5.13	-2.04	7.17

		-264.37	5.16	-2.17	7.33
		-264.36	5.13	-2.20	7.33
		-264.26	5.02	-2.30	7.32
		-264.26	4.98	-2.05	7.03
		-264.34	5.06	-2.25	7.31
Kinks	0.84*	-265.26	4.48	-2.40	6.88
		-265.66	4.29	-2.27	6.57
		-265.62	4.30	-2.08	6.39
		-265.06	4.64	-2.31	6.94
		-265.54	4.42	-2.44	6.86
		-265.58	4.24	-2.25	6.50
		-265.60	4.31	-2.18	6.49
		-265.34	4.42	-2.35	6.77
		-265.40	4.38	-2.27	6.65
		-265.17	4.52	-2.45	6.97
Amorphous regions	0.94*	-265.02	5.02	-1.32	6.34
		-264.97	5.26	-1.37	6.63
		-264.86	5.32	-1.24	6.56
		-265.06	5.25	-1.41	6.66
		-264.97	5.29	-1.11	6.40
		-264.86	5.27	-1.32	6.60
		-264.97	5.29	-1.11	6.40
		-265.02	5.22	-1.38	6.60
		-264.96	5.26	-1.24	6.51
		-264.88	5.35	-1.33	6.68
		-264.88	5.35	-1.33	6.68
Lamella	0.99*	-264.74	5.26	-1.09	6.34
		-264.68	5.16	-1.04	6.20
		-264.65	5.20	-1.16	6.36
		-264.73	5.22	-1.15	6.36
		-264.72	5.37	-1.17	6.54
		-264.71	5.16	-0.96	6.12
		-264.71	5.20	-1.11	6.30
		-264.72	5.21	-1.15	6.36
		-264.69	5.25	-1.14	6.40
		-264.67	5.19	-1.16	6.35
Semi-Crystalline	0.97*	-264.85	5.15	-1.08	6.24
		-264.80	5.20	-1.08	6.27
		-264.96	5.01	-1.15	6.17
		-264.78	5.16	-1.01	6.17
		-264.81	5.32	-1.21	6.53
		-264.74	5.37	-1.20	6.57
		-264.75	5.08	-0.97	6.05
		-264.79	5.30	-1.12	6.42
		-264.80	5.08	-0.95	6.03
		-264.82	5.03	-1.09	6.12

*Average density.

Table B.3: Computed PBE E_{C1s}, and HSE06 CBM, VBM and E_{g} of PE with chemical defects, given in eV.

Chemical Defects	E_{C1s}	CBM	VBM	E_{g}
C=C	-264.26	4.53	-1.74	6.26
C=C-C=C	-264.30	3.49	-1.17	4.66
C=CH2	-264.72	2.39	0.25	2.14
C=O	-264.11	3.71	-2.29	5.99
OH	-264.10	5.14	-2.69	7.83
O=C-OH	-263.70	4.15	-2.61	6.75
C-O-C	-264.15	5.13	-2.05	7.18
O-C-O	-264.31	4.92	-2.45	7.37
C-I	-263.92	4.08	-1.58	5.65
C-Br	-263.87	4.53	-2.24	6.78
C-Cl	-263.58	5.03	-2.70	7.74

Table B.4: 50 data points used to train the relationship between $E_{\mathrm{g}}^{\mathrm{PBE}}$ and $E_{\mathrm{g}}^{\mathrm{HSE06}}$ (Eq. 2.1).

Data points	$E_{\mathrm{g}}^{\mathrm{PBE}}$	$E_{\mathrm{g}}^{\mathrm{HSE06}}$	Data points	$E_{\mathrm{g}}^{\mathrm{PBE}}$	$E_{\mathrm{g}}^{\mathrm{HSE06}}$
1	6.87	8.28	26	5.60	6.86
2	6.58	7.98	27	5.27	6.50
3	6.65	8.06	28	5.27	6.49
4	6.66	8.05	29	5.51	6.77
5	6.53	7.89	30	5.39	6.65
6	6.49	7.86	31	5.57	6.88
7	6.47	7.82	32	5.57	6.83
8	6.52	7.91	33	5.19	6.40
9	6.47	7.85	34	5.51	6.76
10	6.55	7.95	35	5.43	6.66
11	6.01	7.33	36	5.48	6.72
12	6.10	7.43	37	5.38	6.64
13	5.86	7.17	38	5.66	6.93
14	6.04	7.33	39	5.57	6.84
15	5.93	7.33	40	5.71	6.98
16	5.97	7.32	41	5.69	6.96
17	5.70	7.03	42	6.76	8.12
18	5.95	7.31	43	6.68	7.99
19	5.62	6.88	44	6.44	7.77
20	5.81	7.13	45	6.30	7.60
21	5.64	6.94	46	6.19	7.47
22	5.57	6.88	47	6.09	7.37
23	5.32	6.57	48	5.79	7.02
24	5.17	6.39	49	5.75	6.88
25	5.66	6.94	50	5.89	6.99

Table B.5: Thermodynamic and optical charge transition levels ($E^{\text{therm}}_{(0/\pm1)}$ and $E^{\text{opt}}_{(0\leftrightarrows\pm1)}$) of chemical defects.

Chemical Defects	$E^{\text{them}}_{(+1/0)}$	$E^{\text{opt}}_{(0\rightarrow+1)}$	$E^{\text{opt}}_{(+1\rightarrow0)}$	$E^{\text{them}}_{(-1/0)}$	$E^{\text{opt}}_{(0\rightarrow-1)}$	$E^{\text{opt}}_{(-1\rightarrow0)}$
C=C	-2.46	-2.76	-2.27	4.17	4.67	3.71
C=C–C=C	-1.98	-2.17	-1.75	3.31	3.67	3.11
$C=CH_2$	-0.15	-0.29	-0.01	3.48	3.60	3.36
C=O	-2.77	-2.82	-2.71	3.87	4.39	3.00
OH	-2.15	-2.16	-2.14	4.97	4.98	4.96
O=C–OH	-1.18	-1.37	-0.84	4.79	5.61	3.81
C–O–C	-2.05	-2.12	-1.98	5.06	5.17	4.87
O–C–O	-2.59	-2.65	-2.54	4.21	4.60	2.94
C–I	-0.51	-0.61	-0.41	5.12	5.83	4.21
C–Br	-1.52	-1.61	-1.44	4.57	5.55	3.33
C–Cl	-1.88	-1.94	-1.83	4.62	5.70	2.97

Table B.6: Computed $\Delta\varphi$ (in, eV) of Al/PE interfaces with three positions of oxygen-containing groups in the second layer of the interface.

Interfaces	parallel	semi-parallel	anti-parallel
Clean Al/PE	-0.20	–	–
Al/PE+O–C–O	-1.67	-1.03	-0.38
Al/PE+OH	-2.40	-1.02	-0.72
Al/PE+C=O	-1.75	-1.64	-1.12
Al/PE+OH–C=O	-2.86	-1.56	-0.25
Al/PE+C–O–C	-2.50	-1.55	-0.80

B.3 Database in Khazana

Computed band gap shown in Table B.2 – B.3 and geometric structures of physical disorder and chemical defects of PE and Al/PE interfaces are also available in Khazana database (http://khazana.uconn.edu/shorturl/pe/). Fig. B.1 shows search results for "polyethylene C=O".

Figure B.1: Search results for “polyethylene C=O”

$C_{24}H_{46}O$ (C=O)

Identification No.	3311 (Record #3310)
Title	Polyethylene (C=O)
Formula, chemical / structural	$C_{24}H_{46}O$ / $C_{24}H_{46}O$
Class	Material class : Polymers & organic materials Geometry class : Point defects (vacancies, interstitials, dopants, adatoms)
Tags	pe_str PE CH2 Polyethylene
Created by	Lihua Chen (lhc0807@gmail.com)
Date uploaded	7 August 2017 02:37:26
Hit	4

DFT Results

Number of Atoms	71
Number of Atom Types	3
Cell Geometry	a = 6.980 Å, b = 9.569 Å, c = 7.673 Å, α = 90.000°, β = 90.000°, γ = 90.000°
Source	L. Chen et al. Sci. Rep. 7. 6128 (2017)
Pseudopotential & XC	PBE
Band Gap, HSE06	5.99 eV
Energy Cutoff	400.00 eV
K-points	4x2x2
Simulation Tool	VASP 5

Structural information in CIF format

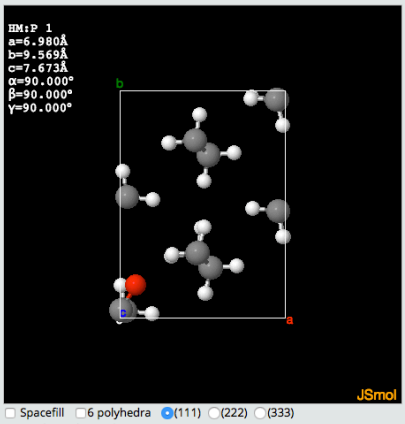

Spacefill 6 polyhedra (111) (222) (333)
3D rendering by Jmol

```
'
==============

# Note: Crystal region of polyethylene
# Common_name: C=O
#------------------------------------------------------------
--------------

data_PE+C=O


_chemical_name_common                  'chemi-CO'
_cell_length_a       6.9803
_cell_length_b       9.5691
_cell_length_c       7.6728
_cell_angle_alpha    90
_cell_angle_beta     90
_cell_angle_gamma    90

_symmetry_space_group_name_H-M    "P 1"
_symmetry_int_tables_number       1

loop_
  _symmetry_equiv_pos_as_xyz
  'x, y, z'

loop_
  _atom_site_label
  _atom_site_occupancy
  _atom_site_fract_x
  _atom_site_fract_y
```

Appendix C

Local Vibrational Density of States

To determine the number of vibrational modes of frequency ω possible in the solid, one spans the $\mathbf{q}$ space within the first Brillouin zone and count the instances when $\omega(\mathbf{q}) = \omega$. This provides the vibrational density of states (DOS), $g(\omega)$, which is mathematically written as:

$$g(\omega) = \frac{1}{N} \sum_{\mathbf{q}} \delta(\omega - \omega_{\mathbf{q}}) \tag{C.1}$$

One can further decompose the contribution of an individual atom towards the vibrational DOS, called the projected DOS (PDOS) [46], using the following relations:

$$g^j(\omega, \hat{\mathbf{n}}) = \frac{1}{N} \sum_{\mathbf{q}} \delta(\omega - \omega_{\mathbf{k}}) |\hat{\mathbf{n}}.\mathbf{e}^j_{\mathbf{q}}| \tag{C.2}$$

$$g^j(\omega) = \sum_{\hat{\mathbf{n}}=n_1,n_2,n_3} g^j(\omega, \hat{\mathbf{n}}) \tag{C.3}$$

where j labels the atom index, $\hat{\mathbf{n}}$ is the unit projection direction vector and $\mathbf{e}^j_{\mathbf{q}}$ is the j^{th} component of the eigenvector corresponding to momentum vector $\mathbf{q}$. One

disadvantage of the above approach is that the DOS data is available only for the entire solid as a whole and not at a specific region within the solid, which maybe particularly relevant when one is interested in the effect of local disorders (such as physical or chemical defects) on the vibrational structure of a solid.

We propose to overcome this challenge by capturing the PDOS information using a gaussian function centered at $\mathbf{r}^g$ and defining the local DOS as:

$$\text{ldos}(\omega, \mathbf{r}^g) = \sum_j c^j g^j(\omega),\ j \in \{|\mathbf{r}^g - \mathbf{r}^j| < r_{\text{cut}}\}, \tag{C.4}$$

where $g^j(\omega)$ is the PDOS of atom j [46] as discussed above and c_j is the weight factor corresponding of atom j at position $\mathbf{r}^j$ and computed using:

$$c^j = \frac{1}{\sqrt{(2\pi\sigma)^3}} \exp^{-\frac{(\mathbf{r}^g - \mathbf{r}^j)^2}{2\sigma^2}} \tag{C.5}$$

where, σ is the length-scale parameter which can be used to tune the width of the gaussian function, or the width of the local region where $\text{ldos}(\omega, \mathbf{r}^g)$ needs to be computed, and the constant before the exponential function is the normalizing factor. The term r_{cut} in Eq. (C.4) is the user-defined cut-off radius beyond which contributions from atoms are ignored and is introduced for computational convenience.